

Egr2 Upregulation Induced Mitochondrial Iron Overload Implicating in Cognitive Deficits after Sevoflurane Administration

Piao Zhang

Zhejiang University

Yeru Chen

Zhejiang University

Shuxia Zhang

Zhejiang University

Man Fang

Zhejiang University

Xianyi Lin

Zhejiang University

Tieshuai Liu

Zhejiang University

Youfa Zhou

Zhejiang University

Xin Yu

Zhejiang University

Gang Chen (✉ chengang120@zju.edu.cn)

Zhejiang University

Research

Keywords: Sevoflurane, Cognitive dysfunction, Early growth response 2, Mitochondrial, Iron overload

Posted Date: November 13th, 2020

DOI: <https://doi.org/10.21203/rs.3.rs-104467/v1>

License: © ⓘ This work is licensed under a Creative Commons Attribution 4.0 International License.

[Read Full License](#)

Abstract

Background: Sevoflurane inhalation initiated cognitive deficits implicated in mitochondrial dysfunction, synaptogenesis impairment and neuroinflammation. Egr2

plays a crucial role in maintaining cognitive function. Therefore, we attempted to clarify the potential correlation regarding Egr2 expression and cognitive deficits induced by sevoflurane administration.

Methods: Animals received sevoflurane anesthesia, and the behavioral tests including Morris water maze, novel object recognition test and trace fear conditioning were performed. Then, the Golgi-Cox staining and Nissl staining were employed to detect the effect of sevoflurane inhalation in hippocampal neurons. Meanwhile, bioinformatics analysis was implemented, and western blot (WB) and bisulfite sequencing PCR (BSP) technique were utilized to validate this hypothesis. Moreover, the level of lipid peroxidation, mitochondrial membrane potential, morphology and membrane permeability, and cytoplasm calcium levels were investigated after Egr2 interference by using JC-1 probe, MitoTracker staining, Mitochondrial permeability transition pore (mPTP) assay, and Fluo calcium indicators, respectively. Additionally, Prussian blue staining was used to evaluate the iron content.

Results: The behavioral tests indicated that the cognitive function was significantly attenuated after sevoflurane administration. The Golgi-Cox staining displayed that the dendritic length, density and nodes were significantly reduced, and the typical neuropathological changes including neuron loss, nucleus shrinkaged and disappearance of Nissl bodies were observed by Nissl staining. Moreover, bioinformatics analysis showed that the Egr2 expression was significantly upregulated, and WB and BSP confirmed this result. Additionally, the results suggested that sevoflurane administration elevated the cytoplasm calcium levels, reduced the mitochondrial membrane potential and triggered the opening of mPTP. Prussian blue staining showed that the iron deposition was apparently increased. However, Egr2 level downregulation partly reversed these above changes.

Conclusion: These findings demonstrated that sevoflurane administration elicited mitochondrial dysfunction and iron dyshomeostasis, and eventually resulted in cognitive impairments, whereas suppressing Egr2 expression partly improved this pathological process.

Introduction

Cognitive dysfunction is one of the most serious complications threatening human health following anesthesia/surgery, which mainly characterized by memory and language deficits, visuospatial and executive dysfunctions, and behavioral disorders [1–3]. Generally, cognitive deficits would result in the loss of independence, a compromised quality of life and increased mortality, and thereby cause heavy economic and mental burden to the society and families [4]. Epidemiological survey showed that approximately 12% of cognitively well patients would develop symptoms of cognitive impairment after anesthesia or surgery [1]. Alcohol abuse, anxious/depressed basal mood, low educational level and genetic susceptibility are identified as the risk factors for cognitive dysfunction [4, 5]. Accumulating

evidence revealed that anesthesia may provoke persistent abnormalities of neuronal circuits by affecting neuronal differentiation and synaptogenesis, and pharmacotoxic effects exacerbated the impairment of cognitive domains [6, 7]. Sevoflurane, as an inhaled volatile anesthetic agent, is widely used in pediatric practice [8]. Previous studies documented that sevoflurane inhalation significantly aggravated cognitive deficits by initiating neuroinflammation and neurotoxicity in rat hippocampus [9]. Sevoflurane administration triggers a series of pathophysiologic reactions comprising of mitochondrial dysfunction [10] and endoplasmic reticulum stress [11], and thereby results in cognitive dysfunction by inducing neuronal apoptosis [12], synaptogenesis impairment [13], and neuroinflammation [14].

Early growth response (EGR) genes are composed of four members (egr-1, egr-2, egr-3, and egr-4), which participate in synaptic and neuronal responses to external stimulation [15]. Of special note are that Egr2 facilitates robustly and sustainedly the maintenance of learning and memory by mediating the synaptic plasticity [16]. Meanwhile, related research suggested that Egr2 was involved in neural activity, synaptic transmission and nervous system development [17]. More interestingly, studies indicated that the motor capacity, exploratory behavior and emotional reactivity were no apparent damage, while the performance of motor learning and object recognition memory was enhanced in Egr2-deficient mice [18]. Therefore, we speculated that Egr2 may implicate in the maintenance of cognitive function after sevoflurane inhalation. Furthermore, many intriguing studies showed that iron accumulation was closely correlated to the pathogenesis of neurodegenerative disorders including Alzheimer disease, Parkinson disease, and degenerative conditions [19]. Iron plays a crucial role in energy metabolism by mediating electron transport chain, ATP production and oxygen consumption [20]. However, excess iron in brain alters the behavior and mood [21], and causes the learning and memory deficits [22]. Mitochondrion, as a cellular organelle, participates in numerous bioenergetic, biosynthetic, and regulatory processes including oxidation-reduction reactions, DNA synthesis and repair [23]. Mounting evidence demonstrated that the dramatic morphological changes of mitochondria result in abnormal absorption and transport of iron, and thereby activate a serial cascade of inflammatory responses [24]. In this study, the potential mechanism regarding sevoflurane administration induced cognitive dysfunction was further investigated. These findings revealed that sevoflurane inhalation induced the morphological alteration of mitochondria and iron metabolism abnormality, and consequently contributed to the neuroinflammation and cognitive dysfunction associated with Egr2 expression, which were conducted to comprehensively illustrate the underlying mechanism and develop appropriate therapeutic strategy for attenuating cognitive deficits following sevoflurane administration.

Materials And Methods

Animals and Ethical statement

Neonatal C57BL/6 mice were purchased from Shanghai Laboratory Animal Center (Chinese Academy of Sciences, Shanghai, China). All experimental operations were in accordance with guidelines for laboratory animal care and safety from NIH, and approved by the Animal Care and Use Committee of Zhejiang

University. All animals were housed with free access to water and chow in appropriate environmental conditions (temperature: 22-25°C, humidity: 45-50%, and 12 h light/dark cycle).

Experiment grouping and treatment

All animals were randomly assigned to different groups according to the experimental protocols: **Part1**) control group (Ctrl) and sevoflurane group (SEV); **Part2**) GFP-Ctrl group, GFP-SEV group, GFP-Egr2 shRNA-Ctrl group, GFP-Egr2 shRNA-SEV group. To induce general anesthesia, the pups were placed in an acrylic anesthetizing chamber with two interfaces including sevoflurane vaporizer and multi-gas monitor. The SEV group was exposed to 3% sevoflurane delivered in humidified 60% O₂ carrier gas for 2 h (2 L/min fresh gas for 3 min, followed by 1 L/min) by using the Datex-Ohmeda anesthesia system (Madison, WI, USA), while the Ctrl group received 60% oxygen (balanced with nitrogen) for the same period at postnatal day 6-8 (P6-8) [10]. Similarly, GFP-Ctrl group and GFP-Egr2 shRNA-Ctrl group received the same process with Ctrl group, and the GFP-SEV and GFP-Egr2 shRNA-SEV group underwent the scheme with SEV group. Moreover, to ensure sufficient ventilation, a single sample (100 µL) of arterial blood was obtained at the end of sevoflurane anesthesia or sham exposure by cardiac puncture from five mice of each group. These animals were not used for any other part of the study. Arterial carbon dioxide partial pressure (PaCO₂), arterial oxygen pressure (PaO₂), blood oxygen saturation (SaO₂) and power of hydrogen (pH) were evaluated by using a blood gas analyzer (Kent Scientific Corp., Torrington, CT, USA) (Table S3). There was no significant difference in pH, PaCO₂, PaO₂, Glucose and SaO₂ level between the groups.

To downregulate Egr2 expression, transfection with adeno-associated virus was performed. Briefly, recombinant adeno-associated virus (AAV) were purchased from Vigene Biosciences company (Shangdong, China), which included either shRNA control (scrambled sequence) or shEgr2 and enhanced green fluorescence protein (EGFP) gene. For Egr2 shRNA viral packaging, the shRNA sequence of mouse Egr2 (5'-GATCCGGGCAGGACAAAGCAATATTGTTCAAGAGACAATATTGCTTTGTCCTGCCCTTTTTTA-3') was synthesized and cloned into pAV-U6-GFP plasmid to produce pAV-U6-eGFP-Egr2 shRNA. Viral particles were purified by iodixanol step-gradient ultracentrifugation. The genomic titer was 4.72×10^{13} TU/mL determined by quantitative PCR. For viral injection, mice were anesthetized with ketamine (100 mg/kg) and xylazine (8 mg/kg) by intraperitoneal injection and placed in a stereotactic frame. Purified and concentrated lentivirus was injected bilaterally into the hippocampus (100 nL, coordinates from bregma \bar{x} - 1.5 mm anterior/posterior, - 2.07 mm medial/lateral, -1.8 mm dorsal/ventral) through glass micropipettes at a slow rate (10 nL/min). The GFP-Ctrl group and GFP-SEV group received AAV9-U6-shRNA(scramble)-GFP virus at P9, and the GFP-Egr2 shRNA group and GFP-Egr2 shRNA SEV group received AAV9-U6-Egr2 shRNA-GFP virus at P9, respectively.

Behavioral test

Morris water maze

After the sevoflurane exposure, the spatial memory abilities were evaluated at P40 by using the Morris Water Maze (MWM) test as previously described [25]. A circular black pool (diameter: 120 cm; depth: 21

cm) was filled with opaque water using black non-toxic ink to reach 1.0 cm above the platform surface (diameter, 10 cm), and the water temperature was kept at 22 °C. Meanwhile, an invisible platform (diameter, 10 cm) was fixed in the pool and submerged 1 cm. In the training phase (P40-44), all animals received four training trials per day for a total of four days. The mice were placed into the pool at a random starting position and allowed to discover the hidden platform for 120 s. Mice were guided to the platform if they could not locate the platform within 2 min. The latency time (the time to reach the hidden platform) was recorded for assessing the spatial learning. In the testing phase (P45), the platform was removed, and the mean distance crossed the original platform site, platform-crossing times, and time spent were recorded for measuring memory function, respectively. After each trial, the mice were wiped dry and a heat lamp was used to faster temperature recovering before returning to home cages.

Novel object recognition test

Cognition was measured by the Novel object recognition (NOR) experiment at P35.

The animals are exposed to two identical objects for 20 min, then trained for 5 min during the familiarization phase. Thereafter, the mice are exposed to a single copy of the familiar object and a novel object (test phase) after 24h. The total distance traveled was recorded and the Recognition index was calculated [26]: A recognition index was calculated for each animal and reported as the ratio $TB/(TA + TB)$, where TA = time spent exploring the familiar object A and TB = time spent exploring the novel object B. Recognition memory was evaluated as in the long-term memory test. Exploration was defined as sniffing or touching the object with the nose or forepaws.

Trace fear conditioning

The fear condition test is extensively used to detect the tone's effect on the hippocampus-dependent memory [27]. Briefly, the mice were placed in a sound attenuating fear-conditioning chamber (ACT-100A, Coulbourn Instrumnets, USA), The mice free explored for 2 min in the chamber, and the freezing was recorded as control. Then, the mice received 30s sound (80dB, 1500HZ) as conditioned stimulus, and foot shock (0.7 mA; 2 s) by the floor's steel rods at last 2 s, and keep the sound and the shock stopped at the same time. The mice stayed in the chamber for another 2 min. The training repeated for 5 times. The next day for contextual fear test, the mice were placed into the same chamber and the freezing was recorded for 5 min. After 2h, the mice were placed into another chamber for 3 min, then received the same conditioned stimulus for 3 min. The freezing of mice was recorded all the time. The data of freezing were recorded by Freeze Frame software.

Tissue harvest

Animals were anesthetized with 2% pentobarbital sodium (40 mg/kg, i.p.) at P47. Then, the right atrium was incised and transcardiac perfusion was performed with heparinized 0.9% saline followed by 4% formaldehyde. The brain tissue was extracted and rinsed using 0.9% sodium chloride at 4 °C. The

hippocampus was stripped and fixed in 30% sucrose in 0.1 M phosphate buffers (pH 7.4, 4 °C) for 24-48h, then the specimens were stored in a -80 °C freezer.

Hematoxylin and Eosin staining

The brain sections were rinsed with methanol for 1 min, and incubated with hematoxylin solution (5 min) and eosin solution (20 sec). The fixed tissues were treated with gradient alcohol and xylene, then embedded with resinene for sealing and observing. The images were captured by using a light microscope (Olympus BX61, Japan).

TUNEL Assay

A TUNEL assay was performed to detect the DNA fragmentation caused by cell death in the hippocampus of aged rats. After preparation of sections (6 µm), the TUNEL staining was carried out using an in situ cell death detection kit (YEASEN, 40302ES20) according to the manufacturer instructions. Fluorescence signals were visualized under an epifluorescence microscope. Images were captured with the assistance of Image-Pro Plus 5.0 software, and all the parameters used in this experiment were kept consistent during capturing.

Immunofluorescent staining

Serial coronal slices (20 µm thick) of hippocampus including CA1, CA3 and DG regions were made by using a rotary microtome (Leica, Germany). The sections were placed in a water bath (96 °C, 20 minutes) for antigen retrieval and blocked using 10% bovine serum albumin at room temperature for 1 hour. The sections were incubated with antibody diluent containing goat antibodies against Tuj1 (1:500; Biolegend, A488-435L), GFAP (1:100; ABclonal, A14673) and NeuN (1:1000; Abcam, ab104224) overnight at 4°C. Then sections were rinsed with PBS (3×10 min) followed by incubation with Alexa Fluor™ 488 goat anti-mouse antibody and Alexa Fluor™ 594 goat anti-rabbit antibody for 1 h at room temperature. After rinsing with PBS (6×5 min), fluorescence signals were visualized under an epifluorescence microscope. Images were captured with the assistance of Image-Pro Plus 5.0 software, and all the parameters used were kept consistent during capturing.

Golgi-Cox staining

The morphology of neuronal dendrites and dendritic spines was investigated in the hippocampus by using the Hito Golgi-Cox OptimStain™ PreKit (Hitobiotec Corp. Kingsport, TN, USA). The brain tissues were obtained after sacrifice, and rinsed with Milli Q water. The equal volumes of Solutions A and B were used to impregnate the brain tissues, and the impregnation solution was replaced the following day and stored in darkness (Room temperature, 2 weeks). Then, the brain tissues were transferred to Solution C, which was replaced the following day. The brains were stored at 4 °C for 72 h in the dark. The Brain sections (100 µm thickness) were generated using a cryotome with the chamber temperature set at -19 °C. Each section was mounted on gelatin-coated microscope slides using Solution C. Each section was

mounted on gelatin-coated microscope slides using Solution C. The excess solution on slide was removed using a Pasteur pipette and absorbed with filter papers, then the sections were allowed to dry naturally at room temperature for 3 days. The dried brain sections were processed according to the manufacturer's instructions. Thereafter, the dendrites of CA1 sub region in the hippocampus were observed by using an Olympus BX61 fluorescence microscope (Olympus, Japan).

Nissl staining

Nissl staining was employed to detect the histomorphology changes of hippocampal neurons according to the previously described [28]. Briefly, the sections were incubated with 0.1% toluidine blue at room temperature for 10 min, and rinsed in double distilled water. Then, the sections were dehydrated, cleared and coated by using gradient aqueous alcohol (70%, 95% and 100%), xylene and neutral resins, respectively. Finally, the sections were observed by using an Olympus BX61 fluorescence microscope (Olympus, Japan).

RNA extraction

For the RNA-Seq analysis, the hippocampal tissues were obtained from Ctrl group and SEV group at P6 and P30, respectively. Total RNA was extracted from different group using RNAiso Plus Reagent (TaKaRa, Japan), and purified by RNasey Mini Kit (QIAGEN) based on the manufacturer's protocol. NanoDrop spectrophotometry (Thermo Scientific, Wilmington, USA) was used to detect the RNA concentration, and the integrity was confirmed through electrophoresis. Subsequently, the cDNA synthesis and antisense RNA (aRNA) amplification was performed using Amino Allyl MessageAmp II aRNA Amplification Kit (Ambion, USA). The total RNA was stored at -80°C for future use.

RNA-Seq

A total of 1.5 µg RNA was used as the input material. The clustering of the index-coded samples was performed by using a TruSeq PE Cluster Kit v3-cBot-HS (Illumina) based on the manufacturer's instructions. The library were sequenced using an Illumina HiSeq platform, and paired-end reads were generated followed by cluster generation. Thereafter, these raw reads in the fastq format were processed by using in-house Perl scripts. Low-quality data were discarded by using Trim Galore (http://www.bioinformatics.babraham.ac.uk/projects/trim_galore/). The GC-content and sequence duplication level of the clean reads were calculated, and the clean reads were assembled with Trinity software via the default parameters (<https://github.com/trinityrnaseq/trinityrnaseq/wiki>). Then, the RNA-seq data files were deposited in the NCBI Sequence Read Archive (SRA) database (SRA accession: Not uploaded, to date).

Data analysis by using integrated Differential Expression and Pathway analysis (iDEP) tools

The differentially expressed genes (DEGs) acquired from the RNA-seq-Based expression profiling were analyzed through iDEP (integrated Differential Expression and Pathway analysis) online tools (<http://bioinformatics.sdstate.edu/idep/>). To date, iDEP seamlessly connects 63 R/Bioconductor

packages, 2 web services, and comprehensive annotation and pathway databases for 220 plant and animal species [29]. Briefly, the expression matrix of DEGs (Table 1 and Table 2) was filtered and converted to Ensemble gene IDs, and the exploratory data analysis (EDA) including K-means clustering and hierarchical clustering was performed using the pre-processed data. The pairwise comparison (Ctrl-6d group VS SEV-6d group; Ctrl-30d group VS SEV-30d group) was employed by using the DESeq2 package with a threshold of false discovery rate FDR < 0.05 and fold-change > 2. Additionally, a hierarchical clustering tree and network of enriched GO terms were constructed to visualize the potential connections among DEPs. Gene Set Enrichment Analysis (GSEA) method was used to investigate the related signal pathways activated by sevoflurane administration. Therefore, WGCNA was performed to construct co-expression networks and sub-modules, and the corresponding enriched pathways in selected module were exhibited, respectively.

Gene Ontology and KEGG Pathway Analysis of DEGs

Gene ontology (GO) analysis and Kyoto Encyclopedia of Genes and Genomes (KEGG) pathway were employed to analyze the differentially expressed genes (DEGs) between different groups (Ctrl-6d group VS SEV-6d group; Ctrl-30d group VS SEV-30d group) by using String online tools (<https://string-db.org/cgi/input.pl>). GO analysis was used to annotate genes and gene products including biological process (BP), cellular component (CC) and molecular function (MF). KEGG is utilized for systematic analysis of gene function and related high-level genome functional information of DEGs, which consists of a series of genome and enzymatic approaches and genomic information with higher order functional information [30].

Integration of Protein-Protein Interaction (PPI) Network Analysis and related database

STRING version 10.0 covers 9, 643, 763 proteins obtained from 2031 organisms [31]. The String database (<https://string-db.org/cgi/input.pl>) is used to predict the protein-protein interactions comprising direct/indirect associations. To investigate the potential relationships, String tool was constructed according to the function and pathway enrichment analysis. Moreover, the Genecards website (<https://www.genecards.org>) and The Human Protein Atlas database (<https://www.proteinatlas.org/>) were separately used to determine the expression of Egr2 in the tissues and organs of the human body.

Western blot

The hippocampal tissues, primary cultured neurons and cell lines among different groups were homogenized using RIPA buffer (Beyotime, P0013B) with 1 × protease inhibitor cocktail (Beyotime, P1010). The supernatant was collected by centrifugation (16, 200×g, 10 min), and the protein concentration was measured through a bicinchoninic acid protein assay kit (Beyotime, P0012S). An aliquot of 50 µg protein was separated via SDS-PAGE and transferred to a nitrocellulose membrane, then blocked with 5% nonfat milk in phosphate-buffered saline (PBS, pH 7.4). The membranes were incubated with primary antibodies against Egr2 (1:1, 000; ABclonal, A15053), ACSL4 (1:500; ABclonal, A16848), FTH1 (1:500; ABclonal, A19544), GPX4 (1:1, 000; abcam, ab125066), COX2 (1:1,000; ABclonal, A1253),

DRP1 (1:500; ABclonal, A17069), DMT1 (1:500; ABclonal, A10231), Ferroportin-1 (1:1, 000; abcam, ab78066, Kdm7a (1:500; ABclonal, A8266), actin (1:5, 000; ABclonal, AC026) at 4 °C overnight. Blots were incubated in horseradish peroxidase-conjugated secondary antibodies against rabbit IgG (1:5, 000, CST, 7071 and 7072) for 2 h at room temperature, then subjected to chemiluminescent detection using the SuperSignal West Pico Substrate (34077, Pierce) and exposed to film. Digital images were quantified using densitometric measurements obtained using Quantity One software (Bio-Rad).

Cell culture

Primary hippocampal neurons were cultured by using fetal mice (E17) hippocampi according to a previously described protocol [32]. Briefly, the mice pregnancy for 17 days was anesthetized through 1% isoflurane, and the uterus was exposed and the fetus was removed. The fetal mice were sacrificed and the hippocampi were obtained under a sterile environment. Then, the hippocampi were treated using 0.125% trypsin in Hank's buffer (in mmol/L: 137 NaCl, 5.4 KCl, 0.4 KH₂PO₄, 0.34 Na₂PO₄·7H₂O, 10 glucose and 10 HEPES) for 12 min at 37 °C and dissociated by repeated passage with Pasteur pipettes. The nerve cells (2 × 10⁵/cm²) were seeded onto poly-L-lysine (10 µg/mL)-coated plates added culture reagents including Neurobasal Medium (Invitrogen), 2% B27 (Invitrogen), 10 U/mL penicillin, 10 U/mL streptomycin, and 0.5 mmol/L glutamine. Hippocampal neurons were cultivated in appropriate environment (37 °C, 5% CO₂). The cells were continuous cultured for 20 d, then harvested for subsequent experiments. Moreover, the cell lines consisting of H4 human neuroglioma were obtained from the China Center for Type Culture Collection. These cells were cultured using Dulbecco's Modified Eagle's Medium (DMEM) supplemented with 10% F12 (all from Gibco, Grand Island, NY, USA) and 10% heat-inactivated fetal bovine serum in a humidified incubator (37 °C, 5% CO₂).

Sevoflurane treatment

The cultured cells were placed in an airtight plastic chamber (MIC-101), which was connected to an acrylic anesthetizing chamber with two interfaces including a sevoflurane vaporizer and a multi-gas monitor. The chamber was gassed with 4.1% sevoflurane in the carrier gas (95% air/5% CO₂) for 15 min, and the concentration of sevoflurane was monitored by a gas monitor (PM 8060, Dräger, Lübeck, Germany) [33]. Then, the chamber was sealed and incubated for 6 h at 37 °C. The gas was renewed every 3 h, and the concentration of sevoflurane was confirmed at the end of the incubation. Meanwhile, the control group received the same procedure with air containing 5% CO₂.

Methylation Status Detection

Bisulfite sequencing PCR (BSP) technique was employed to detect the methylation status, which displayed the percentage of methylated CpGs in the potential CpG methylation sites. The original sequence of Egr2 gene was obtained from Genbank database, and the MethPrimer (<http://www.urogene.org/methprimer/index1.html>) was used to predict the corresponding sites of CpG island and primer in the promoter regions, and the primer sequence was designed as follows:

TGGTATTGGGGTTTTTTTTGATTAT (BSP-Egr2-F); AAAACTACCCTACCCTTCTCAACTT (BSP-Egr2-R). The DNA was extracted using the TIANamp Genomic DNA Kit, and the bisulfite-treated DNA was purified after DNA denaturation and bisulfite conversion. The genomic DNA were modified by bisulfite, and the differentially methylated region of Egr2 was amplified by using polymerase chain reaction (PCR). The optimal experimental conditions included: an initial incubation for 2 min at 98°C, followed by 30 cycles of 10 s at 98°C, 30 s at 55°C, and 30 s at 72°C, and finally 2min at 72°C. The PCR product was sequenced, and the Chromas software was used to analyze the sequencing results. The methylation status was determined according to the peak height of cytosine (C) and thymine (T) signals, and the calculation formula was below: The methylation rate of single CpG site (%) = $\frac{\text{Peak height of C}}{\text{Peak height of C} + \text{Peak height of T}} \times 100\%$; The methylation level (%) = $\frac{\text{Methylation rate of total CpG sites}}{\text{Number of CpG sites}}$.

Plasmid and transfection

pAU-U6-shRNA (Egr2) plasmid and pAU-U6-shRNA (Kdm7a) plasmid were purchased from Vigene Biosciences (Shandong, China). pAU-U6-shRNA (Egr2) plasmid used the shRNA sequence: GGGCAGGACAAAGCAATATTGTTCAAGAGACAATATTGCTTTGTCCTGCCCTTTTTT. pEGFP-PARK2, pAU-U6-shRNA (Kdm7a) plasmid used the shRNA sequence: GGATTTGATGTCCCTATTATTTCAAGAGAATAATAGGGACATCAAATCCATTTTTT. The plasmids pAU-U6-shRNA (Egr2) and pAU-U6-shRNA (Kdm7a) were transfected into H4 cells using Lipofectamine 3000 reagent following the specific protocol for this cell line.

Iron Levels detection

Iron assay was performed according to the manufacturers' protocol of Iron Assay Kit (Abcam, ab83366) [34]. Briefly, the specimens were incubated with iron reducer at 25 °C for 30 min followed by incubating for 60 min with iron probe at 25 °C. Then, the microplate reader (OD 593 nm) was used to detect the level of iron.

Lipid peroxidation assay

To detect the level of lipid peroxidation, the fluorescent reporter molecule C11-BODIPY^{581/591} (Invitrogen™, D3861) was used. Cells were induced with the probes for 30 min (2.5 μM), and the fluorescence of C11-BODIPY^{581/591} shifted from red to green. The fluorescence spectrophotometer was utilized to monitor this kinetics of the reaction, and the fluorescence emission intensity at 520 nm was recorded. Images were captured with the assistance of Image-Pro Plus 5.0 software, and all the parameters used were kept consistent during capturing.

Detection of mitochondrial membrane potential and calcium level

Mitochondrial membrane potential was detected by using JC-1 (Thermo Fisher Scientific, MA, USA) fluorescent dye. H4 cells were randomly divided into four groups including Ctrl group, SEV group, Egr2

shRNA group and SEV+ Egr2 shRNA group, and these cells were cultured for 6 h. Then, 10 μ M JC-1 reagent was added and stained for 20 min. JC-1 emits fluorescence including red fluorescent J-aggregates (530 nm excitation/590 nm emission) at high potentials, and green fluorescent J-monomers (490 nm excitation/530 nm emission) at low potentials. The cells were visualized immediately after treatment using an epifluorescence microscope. Images were captured with the assistance of Image-Pro Plus 5.0 software.

Additionally, the cytoplasmic calcium level was measured using Fluo calcium indicators (Fluo-4, AM, YEASEN, 40704ES50). An aliquot of DMSO stock solution (5 mM) was diluted to a final concentration of 5 μ M in buffered physiological medium. H4 cells were washed with indicator-free medium after treating for 6 h. The fluo acetoxymethyl ester was used for cell incubation (30-60 min, 37°C). Cells were washed in indicator-free medium once again prior to fluorescence was measured. The fluorescence signals were visualized by an epifluorescence microscope after treatment. Images were obtained with the assistance of Image-Pro Plus 5.0 software.

MitoTracker Imaging

H4 cells were randomly divided into four groups consisting of Ctrl group, SEV group, Egr2 shRNA group and SEV+Egr2 shRNA group, and these cells received corresponding treatment for 6 h. The medium was replaced with pre-warmed (37°C) 50 nM MitoTracker (Invitrogen) medium for 10 min. Thereafter, the loading solution was replaced with fresh medium once again. The cells were visualized after treatment by using an epifluorescence microscope. Images were captured with the assistance of Image-Pro Plus 5.0 software.

Mitochondrial permeability transition pore assay

Mitochondrial transition pore assay kit (C2009S, Beyotime, China) was used to visualize the mitochondrial transition pores according to the manufacturer's instructions. Cells were stained using acetoxymethyl ester of calcein dye (calcein AM, green) followed by incubating with CoCl_2 solution, which effectively quenched the calcein fluorescence in the cytoplasm. The calcein fluorescence could not be quenched if the MPTP is tightly closed, while the Co^{2+} ions enter the mitochondria to quench the mitochondrial calcein fluorescence when the MPTP is open. Mitochondrial pore opening reduced the green fluorescence.

Determination of Malondialdehyde (MDA) and GSH Levels

Tissue proteins were prepared as described in the Lipid Peroxidation MDA assay kit (Beyotime, S0131). The MDA concentration of each sample was evaluated by multimode microplate readers (Spectramax M5) at 532 nm, and using 490 nm served as a control. Additionally, the level of GSH were measured according to the requirements of the instructions in reagent kits (Beyotiome, S0052), and the protein concentration was determined with BCA protein assay reagent kit. The values were normalized to total protein in tissue samples.

Reactive oxygen species determination

H4 human neuroglioma cells were randomly divided into four groups including Ctrl group, SEV group, Egr2 shRNA group and SEV+ Egr2 shRNA group, and the regional mitochondrial ROS accumulation was measured by using the Mito-SOX reagent (M36008, Thermo Fisher, USA). After treatment, H4 cells were washed with HBSS solution buffer. A 5 μ M Mito-SOX working solution was then prepared. Next, 1.0 mL of the 5 μ M Mito-SOX reagent was applied as a cell loading solution in which cells were incubated for 10 min at 37 °C without light exposure. Cells were then gently washed three times with warm PBS. Excitation wavelengths were measured at 510 nm and emission at 580 nm by a fluorescence microplate reader (SpectraMax M5/M5e). The intracellular ROS levels in H4 cells were measured with the fluorescent probe dihydroethidium (DHE). After being treated with 4.1% sevoflurane for 6 h, H4 cells were incubated with 1 μ M DHE (YEASEN, 50102ES02, China) for 60 min at 37°C. Excitation wavelengths were measured at 518 nm and emission at 610 nm by a fluorescence microplate reader (SpectraMax M5/M5e).

Mitochondrial respiration analysis

The oxygen consumption rate (OCR) was measured by using a Seahorse XF96 analyzer (Seahorse Agilent, USA) combined with the Agilent Seahorse XFe96 Extracellular Flux Assay Kit according to the manufacturer's recommendations. Briefly, H4 cells were seeded in 96-wells of a Agilent Seahorse XF96 cell culture microplate (101085-004) and received corresponding treatment for 6 h. The culture medium was replaced with 175 μ L assay medium, supplemented with 25 mM glucose, 2 mM glutamine, and 2 mM pyruvate on the day of the assay. Prior to the assay, plates were incubated at 37°C for approximately 1 h in a non-CO₂ incubator. Afterwards, the basal OCR was determined followed by the automated injection of 25 μ L oligomycin (8 μ M), and mixing for 3 min and measurement for 2 min. Next, 25 μ L carbonyl cyanide 4-(trifluoromethoxy) phenylhydrazone (FCCP) (9 μ M) was injected, and OCR was measured for 2 min. Finally, a combination of 25 μ L rotenone (20 μ M) + antimycin A (100 μ M) was injected, followed by the same mixing and measurement steps. ECAR was automatically recorded by the Seahorse XFe96 software, and the respiration rate was calculated by the Seahorse analyzer.

MitoTracker and ERTracker Imaging

H4 cells were randomly divided into four groups (Ctrl group, SEV group, Egr2 shRNA group and SEV+ Egr2 shRNA group), and these cells received corresponding treatment for 6 h. Thereafter, the medium was replaced with prewarmed (37 °C) MitoTracker medium (50 nM, Invitrogen) for 5 min and ERTracker medium (100 nM invitrogen) for 30 min. cells were permeabilized with 0.2% Triton® X-100 for 10 minutes and incubated with antibody diluent containing goat antibodies against Drp1 (1:100; ABclonal, A17069) overnight at 4 °C. Then sections were rinsed with PBS (3×10 min) followed by incubation with Alexa Fluor™ 594 goat anti-rabbit antibody for 1 h at room temperature. After rinsing with PBS (6×5 min), fluorescence signals were visualized under an epifluorescence microscope. Images were captured with the assistance of Image-Pro Plus 5.0 software, and all the parameters used were kept consistent during capturing.

Morphological observation of mitochondria

The hippocampal tissues were fixed with 2.5% glutaraldehyde overnight at 4 °C, and post-fixed with 1% osmium tetroxide for 2 h after rinsing for three times with phosphate-buffered saline (PBS). Then, the specimens were rinsed with distilled water followed by a graded ethanol dehydration series ending with propylene oxide. After infiltration in a mixture of one-half propylene oxide and one-half resin, the tissues were embedded in resin. Cross sections (120 nm) were made, which were stained with 4% uranylacetate for 20 min and 0.5% lead citrate for 5 min. The morphology of mitochondria in the hippocampal neurons was observed by using a transmission electron microscope (TEM) (Phliphs Tecnai 10, Holland) in the Center of Cryo-Electron Microscopy at Zhejiang University.

Prussian blue staining

Sections (5 µm) were stained for Prussian blue reaction through an Iron Stain Kit (YEASEN, 60533ES20) according to the manufacturer's instructions. Briefly, slides were deparaffinized and hydrated to deionized water. Then, the samples were immersed in a freshly prepared solution of equal parts 5% potassium ferrocyanide and 5% hydrochloric acid for 10 min. Meanwhile, the samples were rinsed using deionized water, immersed in 2% pararosaniline solution for 5 min, and rinsed with deionized water once again, and immediately dehydrated and coverslipped. Images of positively stained sections were captured via an Olympus BX61 microscope.

Quantitative real-time PCR (qRT-PCR)

H4 cells were randomly divided into four groups (Ctrl group, SEV group, Kdm7a shRNA group and SEV+Kdm7a shRNA group), and these cells received corresponding treatment for 6 h. Briefly, the total RNA of the H4 cells was isolated with TRIzol reagent (TRANS, ER501-01), and reverse transcribed to cDNA using the Revert Aid TM First Strand cDNA Synthesis kit (Vazyme, R233-01) according to the manufacturer's protocol. The forward and reverse primer sequences was shown below: F) ACAGTAACTGGAAGCTGCCTCTGTTG; R) AACTCACTCTGTAGGCCAGGC. PCR amplification was performed as follows: 95°C for 5 min; 40 cycles, 94 °C for 60 s, 62°C for 1 min, 72°C 1 min; 72°C 10min. The results were analyzed with 480II Real-Time PCR System software (Roche). The level of actin was used as an internal standard. Each assay was performed in triplicate.

Detection of Methylated DNA level

H4, BV-2 and N2A cells were randomly divided into four groups (Ctrl group, SEV group, Kdm7a shRNA group and SEV+Kdm7a shRNA group), and these cells received corresponding treatment for 6 h. Thereafter, Methylated DNA quantification kit (abcam, ab117128) was utilized to determine the level of Methylated DNA. Triple independent experiments were performed for each group.

Statistical analysis

SPSS 19.0 software was used to process the data. All data are represented as mean \pm standard deviation, and analyzed by one-way analysis of variance (ANOVA) and Tukey's post hoc test. $P < 0.05$ was considered statistically significant.

Results

Sevoflurane Exposures induced Cognitive Impairment in developing mice

To determine the effect of sevoflurane administration on cognitive function, behavioral tests including Morris Water Maze, novel object recognition test and trace fear conditioning were performed. The results showed that the time course of mean escape latency was longer at fourth and fifth day in SEV group than that of in Ctrl group (Fig. 1A, $P < 0.05$). The time spent in the target quadrant and the total number of platform area crossings were significantly decreased in SEV group compared to Ctrl group (Fig. 1B-C, $P < 0.05$). The fear condition test showed that the freezing time was dramatically reduced in SEV group than that of in Ctrl group (Fig. 1D-F, $P < 0.05$). The novel object recognition test suggested that the overall distance of traveling was no significant different (Fig. 1G, $P > 0.05$), while the recognition index was decreased in SEV group compared to Ctrl group (Fig. 1H, $P < 0.05$).

Sevoflurane administration induced the neuronal death and reduced the synapse formation in hippocampus

HE staining could well display the structural alterations in the hippocampal neurons. In this study, the results showed that the Ctrl group have round nuclei and are palely stained (Fig. 1K). On the contrary, neuronal morphological changes including chromatic agglutination, karyopyknosis, and dyeing darker were observed in the SEV group (Fig. 1K). Meanwhile, the neuronal cell counts were obviously reduced in DG, CA1 and CA3 region of SEV group when compared with Ctrl group, respectively (Fig. 1J, $P < 0.05$). Meanwhile, the TUNEL assay was used to visualize the apoptosis, and the results showed that the apoptosis rate was significantly increased in SEV group including DG, CA1 and CA3 region than that of in Ctrl group (Fig. 2C). Moreover, the presence of neuron-like cells was detected in the hippocampal tissue by using antibodies against Tuj1 and NeuN. The immunofluorescence staining results showed that the Tuj1-positive cells were obviously increased, while the NeuN-positive cells were decreased in SEV group including DG, CA1 and CA3 region compared to Ctrl group (Fig. 2A, B). Additionally, the results displayed that the dendritic length, density and nodes were significantly reduced after sevoflurane administration compared with Ctrl group indicated by Golgi-Cox staining (Fig. 2D). And Nissl staining results showed that the typical neuropathological changes including neuron loss, nucleus shrinkaged and disappearance of Nissl bodies were observed in SEV group compared to that of in Ctrl group (Fig. 2E). Moreover, the quantitative results showed that the relative fluorescence intensity of Tuj1 and the positive cell counts by Tunal staining were significantly increased in SEV group than that of in Ctrl group (Fig. 2F, H; $P < 0.05$). Whereas, the relative fluorescence intensity of GFAP and NeuN and the number of dendritic spines were obviously reduced in SEV group compared to Ctrl group (Fig. 2F, G, I; $P < 0.05$).

Bioinformatics Analysis For Rna-seq Data

To further clarify the potential mechanism, RNA-Seq was performed and the data were analyzed by using integrated Differential Expression and Pathway analysis (iDEP) tools and String database (<https://string-db.org/cgi/input.pl>). Firstly, iDEP correctly recognized samples according to the number of matched genes IDs after uploading the read count data. The gene ID was converted and filtered. Figure (3 A, B) showed the distribution of the transformed data, and Fig. (3 C) suggested that the variation among replicates was small. Then, all genes were ranked based on the standard deviation, and the hierarchical clustering was drawn across all samples using the top 100 genes (Table 3). The graph showed that sevoflurane administration induced significant changes of genes expression (Fig. 3D). The top 100 genes were divided into four groups by using k-means clustering according to the within-group sum of squares plot, and the Figure (3 E, F) showed the four gene clusters and the enriched GO terms, and the data details were attached to table S1 and S2, respectively. The result indicated that these genes mainly participated in the nervous system development including neuron differentiation and projection, neurogenesis and so on (Figure. 3F, Table S2). Thereafter, Parametric Gene Set Enrichment Analysis (PGSEA) was performed, and the Figure (3 G, H) separately showed the potential interaction networks and signaling pathways involved in DNA replication and cell cycle. Moreover, weighted gene correlation network analysis (WGCNA) was employed to investigate the potential correlations amongst genes and groups by using network topology, and the results showed that these genes were clearly delineated 12 modules (Figure. 3I).

Sevoflurane Administration Results In The Egr2 Expression Upregulation

The differential expression genes (DEGs) including 3 upregulated and 18 downregulated genes were screened by using IDEP tools with $FDR < 0.05$, $Fold\ Change > 2$, and the heat map was showed in Fig. 4A, and these genes were enriched in various signal pathways consisting of learning or memory (Fig. 4B). Then, these hub genes were further analyzed through String database. Briefly, the GO function analysis as a dynamic controlled vocabulary is utilized to describe the role of gene with three categories information comprising of biological process (BP), cellular component (CC), and molecular function (MF). GO term enrichment analysis indicated that the BP was involved in 88 categories, and the top 10 BP was presented in Fig. 4C; the CC consists of 2 categories showed in Fig. 4D; and the MF includes 17 categories, and the top 10 MF was showed in Fig. 4E. Meanwhile, the PPI network analysis was constructed for DEGs, and the results were showed in Fig. 4F, and the enriched pathways of DEGs were showed in Fig. 4H. And the volcano plot showed the distribution of DEGs according to the Fold Change and P value (Fig. 4G, Table 4). Gene coexpression was visualized by String tools, which revealed that Arc and Egr2 were coexpression in human beings and *Mus musculus*. The previous researches indicated that Arc genes were participated in the regulation of synapse formation [35, 36], then we speculated that Egr2 may involve in the central nervous development and the maintenance of learning and memory according

to the related references. The results showed that the expression level of Egr2 was significantly upregulated in SEV group compared to Ctrl group at P6 and P30 (Fig. 4J). The Genecards database (<https://www.genecards.org>) was used to search the mRNA expression in normal human tissues from GTEx, Illumina, BioGPS, and SAGE (Serial Analysis of Gene Expression) for EGR2 Gene. Meanwhile, The Human Protein Atlas website (<https://www.proteinatlas.org/>) was utilized to retrieve this Egr2 expressional data separately obtained from Consensus Human Brain Dataset, GTEx Human Brain RNA-Seq Dataset and FANTOM5 Human Brain CAGE Dataset. And the results showed that the expression level of Egr2 was low specially in hippocampal formation (Fig. 4K-N). Similarly, the WB results indicated that the relative protein level of Egr2 was significantly increased in SEV group when compared with Ctrl group in animal hippocampus and primary cultured neuron, respectively (Fig. 4O, P; $P < 0.05$). Furthermore, bisulfite sequencing PCR (BSP) technique was employed to detect the methylation status, and the results displayed that the percentage of methylated CpGs was significantly reduced in SEV group compared to Ctrl group (Fig. 4Q; $P < 0.05$).

Egr2 downregulation alleviated the cognitive deficits induced by sevoflurane administration

To determine the effect of Egr2 downregulation in cognitive function, Morris water maze and Trace fear conditioning were performed. The results showed that there were no significant different among the time course of mean escape latency, the time spent in the target quadrant and the total number of platform area crossings in GFP-Egr2 shRNA-Ctrl group when compared with GFP-Ctrl group (Fig. 5A-C; $P > 0.05$). However, the time course of mean escape latency was reduced in GFP-Egr2 shRNA-SEV group compared to GFP-SEV group at third and fourth day (Fig. 5A; $P < 0.05$); and the time spent in the target quadrant and the total number of platform area crossings were obviously increased in GFP-Egr2 shRNA-SEV group when compared with GFP-SEV group (Fig. 5B, C, I; $P < 0.05$). The memory retrieval test showed that there were no differences in the freezing response between GFP-Ctrl group and GFP-Egr2 shRNA-Ctrl group (Fig. 5D-F; $P > 0.05$). Whereas, the freezing time was significantly increased in GFP-Egr2 shRNA-SEV group compared to GFP-SEV group (Fig. 5D-F; $P < 0.05$). The novel object recognition test displayed that there were no significant different in overall travelled distance among four groups (Fig. 5G; $P > 0.05$), and the recognition index was reduced in GFP-SEV group when compared to GFP-Ctrl group, while which was increased in GFP-Egr2 shRNA-SEV group compared with GFP-SEV group (Fig. 5H, $P < 0.05$).

The Fig. (5 J) showed that the recombinant adeno-associated virus (AAV) was transfected into the hippocampus by intracerebroventricular injection assisted with stereotaxic apparatus, and the green fluorescence suggested that the AAV successfully reached the ventricular injection sites. Meanwhile, the WB assay results showed that the Egr2 protein level was significantly elevated in GFP-SEV group than that of in GFP-Ctrl group (Fig. 5K, $P < 0.05$). Whereas, the Egr2 protein level was obviously decreased in GFP-Egr2 shRNA-SEV group compared to GFP-SEV group (Fig. 5K, $P < 0.05$). Similarly, the results of Golgi-Cox staining indicated that the dendritic length, density and nodes were significantly increased in GFP-Egr2 shRNA-SEV group compared to that of in GFP-SEV group, while which was no significant different between GFP-Egr2 shRNA-Ctrl group and GFP-Ctrl group (Fig. 5L).

Sevoflurane Administration Elicits Iron Overload And Mitochondrial Dysfunction associated with Egr2 upregulation

The results showed that the protein level of ACSL4 and COX2 was upregulated, but the GPX4 and FTH1 protein level was downregulated in SEV group compared with that of in Ctrl group (Fig. 6A). Meanwhile, the protein level of ACSL4 and COX2 was upregulated, while the GPX4 and FTH1 protein level was downregulated in GFP-Egr2 shRNA-SEV group compared with GFP-Ctrl group in neuron and hippocampus, respectively (Fig. 6B, C). Whereas, the protein level of ACSL4 and COX2 was reduced, while the GPX4 and FTH1 protein level was increased in GFP-Egr2 shRNA + SEV group compared to that of in GFP-SEV group in neuron and hippocampus, respectively (Fig. 6B, C). The iron assay showed that sevoflurane administration significantly induced iron overload compared to Ctrl group (Fig. 6D, $P < 0.05$). There was no significant different between GFP-Egr2 shRNA-Ctrl group and GFP-Ctrl group (Fig. 6E, $P > 0.05$). However, the iron content was reduced in GFP-Egr2 shRNA-SEV group compared to that of in GFP-SEV group (Fig. 6E, $P < 0.05$). To detect the level of lipid peroxidation, the fluorescent reporter molecule C11-BODIPY^{581/591} was used. The results showed that the fluorescence partly shifted from red to green after sevoflurane administration (Fig. 6F). The quantitative results showed that the red fluorescence was decreased and green fluorescence was increased in SEV group compared with that of in Ctrl group (Fig. 6F, G; $P < 0.05$). However, the red fluorescence was increased and green fluorescence was decreased in SEV + Egr2 shRNA group compared to SEV group (Fig. 6F, G; $P < 0.05$).

Mitochondria are the cellular structures responsible for energy metabolism, which mainly correlated to the mitochondrial membrane potential and cytoplasm calcium levels. Therefore, the mitochondrial membrane potential and calcium level were detected by using JC-1 probe and Fluo calcium indicators. The results showed that the red fluorescence was decreased and green fluorescence was increased in SEV group compared with Ctrl group (Fig. 6F, H; $P < 0.05$). Whereas, the red fluorescence was increased and green fluorescence was decreased in SEV + Egr2 shRNA group compared with SEV group (Fig. 6F, H; $P < 0.05$). Moreover, the cytoplasm calcium levels were upregulated in SEV group compared to Ctrl group, while which was downregulated in SEV + Egr2 shRNA group compared with SEV group (Fig. 6J; $P < 0.05$). Mitochondrial morphology was detected by MitoTracker staining, and the representative imaging showed that sevoflurane administration accelerated the formation of fragmentation, reduced volume and intercrystal space in mitochondria compared with Ctrl group, while this status was partly reversed in SEV + Egr2 shRNA group when compared to SEV group (Fig. 6F). Mitochondrial permeability transition pore assay was employed to detect the membrane permeability by observing the fluorescence quenching. The results showed that the green fluorescence was reduced in SEV group than Ctrl group, whereas which was effectively enhanced in SEV + Egr2 shRNA group compared with SEV group (Fig. 6F, I; $P < 0.05$). Meanwhile, the results showed that the concentration of MDA was no significant different between GFP-Egr2 shRNA-Ctrl group and GFP-Ctrl group, but which was obviously decreased in GFP-Egr2 shRNA-SEV group compared to GFP-SEV group (Fig. 6K, $P < 0.05$). Similarly, the level of GSH was decreased in SEV

group than Ctrl group, but which was effectively evaluated in SEV + Egr2 shRNA group compared to SEV group (Fig. 6L, $P < 0.05$). Additionally, the DHE and mito-SOX staining were used to detect the level of intracellular and mitochondrial ROS in H4 cells, respectively. The data suggested that sevoflurane administration obviously enhanced the intracellular ROS level and the mitochondrial ROS level, while Egr2 gene silencing effectively reversed the ROS level in intracellular and mitochondrial compared with SEV group (Fig. 6M, $P < 0.05$). Furthermore, the OCR and ECAR assay were performed to investigate the mitochondrial respiratory function including anaerobic glycolysis and aerobic respiration in H4 cells, respectively. Sevoflurane administration significantly suppressed mitochondrial respiration consisting of reducing aerobic respiration and enhancing anaerobic glycolysis (Fig. 6N, O). Particularly, the ATP production, basal respiration and maximum respiration were obviously decreased in SEV group than Ctrl group, whereas which were significantly elevated in SEV + Egr2 shRNA group compared with SEV group (Fig. 6P-R, $P < 0.05$).

Egr2 downregulation alleviates iron overload-induced ER-mediated mitochondrial fission in hippocampal primary neurons

To investigate the correlation between Egr2 expression and iron overload-induced mitochondrial fission, MitoTracker (Red) and ERTracker (Green), and Drp1 localization were performed. The results showed that sevoflurane administration induced iron overload, and thereby increases the co-localization of Drp1 puncta and expanded ER on mitochondria/fragmented mitochondria in hippocampal neurons when compared with Ctrl group; whereas, the co-localization among Drp1 puncta, expanded ER, and mitochondria/fragmented mitochondria was effectively reduced in SEV + Egr2 shRNA group than SEV group (Fig. 7A, C, $P < 0.05$). Meanwhile, mitochondria presented decreased volume and intercrystal space, and shrunken, and the longest diameter of mitochondria was decreased in SEV group compared with Ctrl group, while those of in SEV + Egr2 shRNA group were significantly improved compared to SEV group (Fig. 7A). Iron distribution was assessed histologically in hippocampus of animals by using Perls' Prussian blue staining. The results showed that the iron deposition was apparently elevated in SEV group than Ctrl group, but which of in SEV + Egr2 shRNA group were effectively reversed when compared to SEV group (Fig. 7A). The WB assay was performed for detecting iron metabolism and mitochondrial fission-related proteins, and the results showed that the protein level of DRP1, DMT1 and Ferroportin-1 was upregulated in SEV group than that of in Ctrl group, while which was downregulated in SEV + Egr2 shRNA group when compared with SEV group (Fig. 7B, $P < 0.05$).

Kdm7a gene expression silencing mediated Egr2 level correlated to the reverse mitochondria dysfunction

The methylated Egr2 was significantly suppressed based on the Bisulfite sequencing PCR detection, then we speculated that methyltransferase was downregulated or demethylase was upregulated. Therefore, Kdm7a gene was screened according to the fold change and P value of RNA-Seq data, and previous reports. The results showed that the mRNA level of Egr2 was decreased in GFP-Kdm7a shRNA-SEV group compared to GFP-SEV group (Fig. 8B, $P < 0.05$), and the protein expression of Kdm7a and Egr2 was obviously upregulated in GFP-SEV group than that of in Ctrl group, whereas which was significantly

downregulated in GFP-Kdm7a shRNA-SEV group compared with GFP-SEV group (Fig. 8A). Meanwhile, the methylated DNA level was detected in H4, BV-2 and N2A cells, respectively. The methylated DNA level was decreased in SEV group compared to Ctrl group, while the Kdm7a shRNA reversed the methylated DNA level after sevoflurane treatment in BV-2, H4 and N2A cells, respectively (Fig. 8C-E; $P < 0.05$). As mentioned above, the mitochondrial morphology, membrane potential, membrane permeability, and cytoplasm calcium levels were measured by MitoTracker staining, JC-1 probe, Mitochondrial permeability transition pore assay, and Fluo calcium indicators, respectively. MitoTracker staining showed that sevoflurane administration facilitated the formation of fragmentation, and reduced volume and intercrystal space in mitochondria compared with Ctrl group, while these changes were effectively improved in SEV + Kdm7a shRNA group compared to SEV group (Fig. 8I). Meanwhile, the red fluorescence was decreased and green fluorescence was increased in SEV group compared to Ctrl group (Fig. 8F, I; $P < 0.05$). However, the red fluorescence was increased and green fluorescence was decreased in SEV + Kdm7a shRNA group compared to SEV group (Fig. 8F, I; $P < 0.05$). Mitochondrial permeability transition pore assay results showed that the green fluorescence was reduced in SEV group compared with Ctrl group, while which was effectively reversed in SEV + Kdm7a shRNA group compared with SEV group (Fig. 8G, I; $P < 0.05$). Furthermore, the cytoplasm calcium level was significantly upregulated in SEV group than Ctrl group, whereas that of in SEV + Kdm7a shRNA group was downregulated compared to SEV group (Fig. 8H, I; $P < 0.05$).

Discussion

Cognitive dysfunction is a common complication involving in learning and memory deficits, attention and information processing anomalies, and personality and social ability disorders [37, 38]. Numerous precipitating factors aggravated the symptoms of POCD comprising of advanced age, genetic susceptibility, prolonged duration of surgery, medications, infectious complications and pain [39]. Related researches revealed that anesthesia accelerated the formation of extracellular amyloid plaques and intraneuronal neurofibrillary tangles, elevated the generation and accumulation of A β , and subsequently exacerbates neurofibrillary degeneration and induced nerve impairment [40]. Previous studies documented that anesthesia inhalation would result in direct toxic effects in neurons by inducing the dysregulation of calcium homeostasis and neurotransmitter release, aggravating the endogenous neurodegeneration processes, and inhibiting the physiological functions of neural stem cells [41]. Currently, sevoflurane was extensively used in pediatric practice as an inhaled volatile anesthetic agent. Emerging evidence demonstrated that sevoflurane administration induced the accumulation of A β , neuroinflammation and neuronal damage, reduced the synaptic plasticity, and eventually resulted in cognitive impairment [42]. In this study, animals received sevoflurane anesthesia at P6-8, then behavioral tests including Morris water maze, novel object recognition test, and trace fear conditioning were performed. The results showed that the the learning and memory performance were significantly impaired following sevoflurane inhalation. Immunofluorescent staining displayed that the immature neurons were increased and the mature neurons were reduced in hippocampus. Golgi-Cox staining displayed that the dendritic length, density and nodes were obviously reduced, and Nissl staining results

suggested that the typical neuropathological changes were induced including neuron loss, nucleus shrinkaged and disappearance of Nissl bodies after sevoflurane administration. Most intriguingly, bioinformatics analysis was employed for RNA-Seq data and the results indicated that the Egr2 expression was closely correlated to the cognitive deficits after sevoflurane administration. Additionally, the level of lipid peroxidation, mitochondrial membrane potential, morphology and membrane permeability, and cytoplasm calcium levels were investigated after Egr2 expression silence, respectively. Our results provide abundant evidence for clarifying the underlying mechanism regarding the cognitive dysfunction induced by sevoflurane administration, which implicated in destroying mitochondrial respiratory network, elevating mitochondria ROS and reducing membrane potential, disturbing calcium homeostasis and iron content, and eventually resulting in neuroinflammation and cognitive impairment.

Mitochondria, as one of the chief sources of reactive oxygen species (ROS), play a crucial role in maintaining normal physiological activities. Excessive stimulation of NAD(P)H and electron transport chain would disrupt the normal redox state of cells and cause the overproduction of peroxides and free radicals, and thereby lead to the oxidative damage and mitochondrial dysfunction [43]. Meanwhile, the mitochondrial DNA impairment derived from accumulation of superoxide radicals would further amplify oxidative stress by mediating critical proteins, and initiating a vicious circle of ROS production to destroy the organelle, induce metabolic disequilibrium and genomic instability, and eventually result in neuronal apoptosis [44–46]. Hippocampus is one of the most vulnerable brain regions to oxidative damage, which is critical for the formation of long-term memory and learning [47]. In this study, the results showed that sevoflurane administration accelerated the formation of fragmentation, reduced volume and intercrystal space, elevated the intracellular ROS level in hippocampal mitochondria, and consequently resulted in the impairment of behavioral outcomes, while Egr2 gene silencing effectively reversed this phenomenon.

Calcium, as a pivotal signaling ion, regulates various physiological/pathological cellular responses involved in eliciting enzyme secretion and activating apoptosis [48]. Calcium overload triggers a serial cascade of pathophysiologic reactions including metabolic disequilibrium, aberrant neurotransmitter release, and disturbing synaptic transmission, which ultimately results in cognitive deficits [49]. Mitochondrial uptake of calcium maintains the intracellular calcium homeostasis, whereas oxidative stress contributes to calcium overload, and in turn activates oxidative metabolism pathways, and thereby triggers the opening of the mitochondrial permeability transition pore (mPTP), and induces the loss of mitochondrial membrane potential and inflammatory response [50]. Egr gene and the pregnenolone sulfate-induced intracellular signaling cascade elicited were closely related to the initial influx of Ca^{2+} [51]. Meanwhile, previous studies showed that the EGR2 expression was reduced after microneme-mediated attachment was blocked using a calcium chelator [52]. And Deltex1 interacted with EGR2 to regulated inflammatory response associated with calcium-NFAT signaling [53]. Interestingly, we found that sevoflurane administration increased the cytoplasm calcium content, reduced the mitochondrial membrane potential and induced the opening of mPTP, while disturbing the Egr2 expression partly improved this status.

Iron is a crucial component for biochemical reactions including cellular metabolism, synthesis of DNA, RNA and proteins, enzymatic reactions, and synthesis of myelin [54]. Emerging evidence revealed that neurons were particularly vulnerable to the alteration of iron content, and iron homeostasis disorder would result in significant neurotoxicity and neurogenetic abnormality, disturbing neurotransmitter synthesis and release, and mitochondrial functions [55]. Generally, free iron could react with oxygen in metabolically active cells to generate hydroxyl radicals and hydroxyl anions, which further participate in chemical implications including lipid peroxidation, DNA strand breaks, and protein modifications and ultimately induce cell death [56]. Simultaneously, previous studies showed that iron participated in the generation of ROS, and caused aggregation and phosphorylation of tau, and thereby aggravated the toxicity by mediating DNA oxidation, lipid peroxidation, accumulation of advanced glycation end products, malondialdehyde and peroxynitrite in Alzheimer patients [57]. Recently, related research proved that sevoflurane disrupted iron homeostasis by affecting the protein expression and mitochondrial iron accumulation [58]. Mitochondria are major generators of iron-sulfur clusters (ISC), and tightly regulated iron uptake and utilization [59]. Additionally, mitochondrion could effectively catalyze electron transport through heme- and ISC-containing proteins to process energy transduction owing to the reversible oxidation states of iron. The prevailing hypothesis indicated that the mitochondrial iron content was affected by the labile iron pool in the cytosol, and Fe^{2+} was transported into the mitochondria by binding with hydrophobic pockets of chaperone proteins [60]. Furthermore, Egr gene was correlated with the HO-1 expression, which could convert heme to iron, and involve in memory, cognition and synaptic plasticity [61]. Egr2 may implicate in stimulating iron acquisition in pro-inflammatory conditions [62]. Consequently, we speculated that Egr2 may play a crucial role in cognitive function correlated to iron metabolism. In this study, the WB assay showed that the protein level of ACSL4, COX2, Ferroportin1 and DMT1 was upregulated, and the GPX4 and FTH1 protein level were downregulated after sevoflurane administration, while which were reversed when Egr2 expression was suppressed. Meanwhile, the iron assay showed that sevoflurane administration significantly induced iron overload, and the iron deposition was apparently elevated in hippocampus indicated by Perls' Prussian blue staining. Therefore, the data strongly supported out hypothesis.

Conclusion

Collectively, these findings documented that oxidative stress induced by sevoflurane administration deranged the mitochondrial respiratory chain and Ca^{2+} homeostasis, and disturbed the mitochondrial membrane-permeability and potential, and further initiated iron dyshomeostasis and neuroinflammation. These changes facilitated the neuronal dysfunction and eventually resulted in cognitive deficiency, whereas suppressing Egr2 expression partly reversed this pathological process.

Abbreviations

AAV Adeno-associated virus

BP Biological process

BSP Bisulfite sequencing PCR

CC Cellular component

DEGs Differentially expressed genes

DMEM Dulbecco's Modified Eagle's Medium

EGR Early growth response

EGFP Enhanced green fluorescence protein

EDA Exploratory data analysis

GO Gene ontology

GSEA Gene Set Enrichment Analysis

iDEP Integrated Differential Expression and Pathway analysis

ISC Iron-sulfur clusters

KEGG Kyoto Encyclopedia of Genes and Genomes

MDA Malondialdehyde

mPTP Mitochondrial permeability transition pore

MF Molecular function

MWM Morris Water Maze

NOR Novel object recognition

OCR Oxygen consumption rate

PGSEA Parametric Gene Set Enrichment Analysis

PBS Phosphate-buffered saline

PCR Polymerase chain reaction

PPI Protein-Protein Interaction

ROS Reactive oxygen species

SRA Sequence Read Archive

WGCNA Weighted gene correlation network analysis

WB Western blot

Declarations

Acknowledgements

We are grateful to the Center for Neuroscience, Zhejiang University for technical and equipment support. And we also thank our funders for providing their support over the past years.

Funding

This research was supported by the National Natural Science Foundation of China (No.81371214 and No.81671063), the Zhejiang Provincial Natural Science Foundation of China (No. LY16H090008 and No. LQ19H030009), and the Key Program of the Natural Science Foundation of Zhejiang, China (No. LZ19H090003).

Author Contributions

PZ, YRC and GC participated in the design of the experimental protocols. PZ, YRC, SXZ, MF and XYL carried out experimental operation. PZ, YRC, TSL and XY were in charge of the data analysis. PZ, YRC and GC drafted the manuscript. All authors read and approved the final manuscript.

Availability of data and materials

Not applicable.

Ethics approval and consent to participate

All experimental operations were in accordance with guidelines for laboratory animal care and safety from NIH, and approved by the Animal Care and Use Committee of Zhejiang University.

Consent for publication

Not applicable

Competing interests

The authors declare that they have no competing interests.

References

1. Needham MJ, Webb CE, Bryden DC. Postoperative cognitive dysfunction and dementia: what we need to know and do. *Br J Anaesth.* 2017;119:i115–25.

2. Kotekar N, Shenkar A, Nagaraj R. Postoperative cognitive dysfunction - current preventive strategies. *Clin Interv Aging*. 2018;13:2267–73.
3. Rundshagen I. Postoperative cognitive dysfunction. *Deutsches Arzteblatt international*. 2014;111:119–25.
4. Ghoneim MM, Block RI. Clinical, methodological and theoretical issues in the assessment of cognition after anaesthesia and surgery: a review. *Eur J Anaesthesiol*. 2012;29:409–22.
5. Ancelin ML, de Roquefeuil G, Ledésert B, Bonnel F, Cheminal JC, Ritchie K. Exposure to anaesthetic agents, cognitive functioning and depressive symptomatology in the elderly. *The British journal of psychiatry: the journal of mental science*. 2001;178:360–6.
6. Flores FJ, Hartnack KE, Fath AB, Kim S-E, Wilson MA, Brown EN, Purdon PL. Thalamocortical synchronization during induction and emergence from propofol-induced unconsciousness. *Proc Natl Acad Sci USA*. 2017;114:E6660–8.
7. Xu L, Hu Y, Huang L, Liu Y, Wang B, Xie L, Hu Z. The association between attention deficit hyperactivity disorder and general anaesthesia - a narrative review. *Anaesthesia*. 2019;74:57–63.
8. Ghatge S, Lee J, Smith I. Sevoflurane: an ideal agent for adult day-case anaesthesia? *Acta anaesthesiologica Scandinavica*. 2003;47:917–31.
9. Tian Y, Chen K-Y, Liu L-D, Dong Y-X, Zhao P, Guo S-B. Sevoflurane Exacerbates Cognitive Impairment Induced by A in Rats through Initiating Neurotoxicity, Neuroinflammation, and Neuronal Apoptosis in Rat Hippocampus. *Mediat Inflamm*. 2018;2018:3802324.
10. Xu G, Lu H, Dong Y, Shapoval D, Soriano SG, Liu X, Zhang Y, Xie Z. Coenzyme Q10 reduces sevoflurane-induced cognitive deficiency in young mice. *Br J Anaesth*. 2017;119:481–91.
11. Liu B, Xia J, Chen Y, Zhang J. Sevoflurane-Induced Endoplasmic Reticulum Stress Contributes to Neuroapoptosis and BACE-1 Expression in the Developing Brain: The Role of eIF2 α . *Neurotox Res*. 2017;31:218–29.
12. Xie S-N, Ye H, Li J-F, An L-X. Sevoflurane neurotoxicity in neonatal rats is related to an increase in the GABA R α 1/GABA R α 2 ratio. *J Neurosci Res*. 2017;95:2367–75.
13. Amrock LG, Starner ML, Murphy KL, Baxter MG. Long-term effects of single or multiple neonatal sevoflurane exposures on rat hippocampal ultrastructure. *Anesthesiology*. 2015;122:87–95.
14. Ji M-H, Qiu L-L, Yang J-J, Zhang H, Sun X-R, Zhu S-H, Li W-Y, Yang J-J. Pre-administration of curcumin prevents neonatal sevoflurane exposure-induced neurobehavioral abnormalities in mice. *Neurotoxicology*. 2015;46:155–64.
15. Li L, Carter J, Gao X, Whitehead J, Tourtellotte WG. The neuroplasticity-associated arc gene is a direct transcriptional target of early growth response (Egr) transcription factors. *Molecular cellular biology*. 2005;25:10286–300.
16. DeSteno DA, Schmauss C. Induction of early growth response gene 2 expression in the forebrain of mice performing an attention-set-shifting task. *Neuroscience*. 2008;152:417–28.

17. Hoban AE, Stilling RM, Moloney G, Shanahan F, Dinan TG, Clarke G, Cryan JF. The microbiome regulates amygdala-dependent fear recall. *Molecular psychiatry*. 2018;23:1134–44.
18. Poirier R, Cheval H, Mailhes C, Charnay P, Davis S, Laroche S. Paradoxical role of an Egr transcription factor family member, Egr2/Krox20, in learning and memory. *Front Behav Neurosci*. 2007;1:6.
19. Rivera-Mancía S, Pérez-Neri I, Ríos C, Tristán-López L, Rivera-Espinosa L, Montes S. The transition metals copper and iron in neurodegenerative diseases. *Chemico-Biol Interact*. 2010;186:184–99.
20. Wessling-Resnick M. Excess iron: considerations related to development and early growth. *Am J Clin Nutr*. 2017;106:1600S–1605S.
21. Kim J, Wessling-Resnick M. Iron and mechanisms of emotional behavior. *J Nutr Biochem*. 2014;25:1101–7.
22. de Lima MNM, Polydoro M, Laranja DC, Bonatto F, Bromberg E, Moreira JCF, Dal-Pizzol F, Schröder N. Recognition memory impairment and brain oxidative stress induced by postnatal iron administration. *Eur J Neurosci*. 2005;21:2521–8.
23. Paul BT, Manz DH, Torti FM, Torti SV. Mitochondria and Iron: current questions. Expert review of hematology. 2017;10:65–79.
24. Jang JY, Blum A, Liu J, Finkel T. The role of mitochondria in aging. *J Clin Investig*. 2018;128:3662–70.
25. Zhong JY, Magnusson KR, Swarts ME, Clendinen CA, Reynolds NC, Moffat SD. The application of a rodent-based Morris water maze (MWM) protocol to an investigation of age-related differences in human spatial learning. *Behavioral neuroscience*. 2017;131:470–82.
26. Lee J, Venna VR, Durgan DJ, Shi H, Hudobenko J, Putluri N, Petrosino J, McCullough LD, Bryan RM. **Young versus aged microbiota transplants to germ-free mice: increased short-chain fatty acids and improved cognitive performance.** *Gut microbes* 2020.
27. Hales JB, Vincze JL, Reitz NT, Ocampo AC, Leutgeb S, Clark RE. Recent and remote retrograde memory deficit in rats with medial entorhinal cortex lesions. *Neurobiol Learn Mem*. 2018;155:157–63.
28. Wang P, Xie Z-D, Xie C-N, Lin C-W, Wang J-L, Xuan L-N, Zhang C-W, Wang Y, Huang Z-H, Teng H-L. AMP-activated protein kinase-dependent induction of autophagy by erythropoietin protects against spinal cord injury in rats. *CNS Neurosci Ther*. 2018;24:1185–95.
29. Ge SX, Son EW, Yao R. iDEP: an integrated web application for differential expression and pathway analysis of RNA-Seq data. *BMC Bioinformatics*. 2018;19:534.
30. Kanehisa M, Goto S. KEGG: kyoto encyclopedia of genes and genomes. *Nucleic Acids Res*. 2000;28:27–30.
31. Szklarczyk D, Franceschini A, Wyder S, Forslund K, Heller D, Huerta-Cepas J, Simonovic M, Roth A, Santos A, Tsafou KP, et al. STRING v10: protein-protein interaction networks, integrated over the tree of life. *Nucleic Acids Res*. 2015;43:D447–52.

32. Zhang CH, Fan YY, Wang XF, Xiong JY, Tang YY, Gao JQ, Shen Z, Song XH, Zhang JY, Shen Y, et al. Acidic preconditioning protects against ischemia-induced brain injury. *Neurosci Lett*. 2012;523:3–8.
33. Zhou Y-F, Wang Q-X, Zhou H-Y, Chen G. Autophagy activation prevents sevoflurane-induced neurotoxicity in H4 human neuroglioma cells. *Acta pharmacologica Sinica*. 2016;37:580–8.
34. Li C, Zhang Y, Cheng X, Yuan H, Zhu S, Liu J, Wen Q, Xie Y, Liu J, Kroemer G, et al: **PINK1 and PARK2 Suppress Pancreatic Tumorigenesis through Control of Mitochondrial Iron-Mediated Immunometabolism**. *Developmental cell* 2018, 46.
35. Béique J-C, Na Y, Kuhl D, Worley PF, Huganir RL. Arc-dependent synapse-specific homeostatic plasticity. *Proc Natl Acad Sci USA*. 2011;108:816–21.
36. Greer PL, Hanayama R, Bloodgood BL, Mardinly AR, Lipton DM, Flavell SW, Kim T-K, Griffith EC, Waldon Z, Maehr R, et al. The Angelman Syndrome protein Ube3A regulates synapse development by ubiquitinating arc. *Cell*. 2010;140:704–16.
37. Kapoor I, Prabhakar H, Mahajan C. Postoperative Cognitive Dysfunction. *Indian journal of critical care medicine: peer-reviewed official publication of Indian Society of Critical Care Medicine*. 2019;23:162–4.
38. Monk TG, Weldon BC, Garvan CW, Dede DE, van der Aa MT, Heilman KM, Gravenstein JS. Predictors of cognitive dysfunction after major noncardiac surgery. *Anesthesiology*. 2008;108:18–30.
39. Wan Y, Xu J, Ma D, Zeng Y, Cibelli M, Maze M. Postoperative impairment of cognitive function in rats: a possible role for cytokine-mediated inflammation in the hippocampus. *Anesthesiology*. 2007;106:436–43.
40. Yang C-W, Fuh J-L. Exposure to general anesthesia and the risk of dementia. *Journal of pain research*. 2015;8:711–8.
41. Wei H, Xie Z. Anesthesia, calcium homeostasis and Alzheimer's disease. *Curr Alzheimer Res*. 2009;6:30–5.
42. Haseneder R, Kratzer S, von Meyer L, Eder M, Kochs E, Rammes G. Isoflurane and sevoflurane dose-dependently impair hippocampal long-term potentiation. *Eur J Pharmacol*. 2009;623:47–51.
43. Liu Y, Yan J, Sun C, Li G, Li S, Zhang L, Di C, Gan L, Wang Y, Zhou R, et al. Ameliorating mitochondrial dysfunction restores carbon ion-induced cognitive deficits via co-activation of NRF2 and PINK1 signaling pathway. *Redox Biol*. 2018;17:143–57.
44. Hollensworth SB, Shen C, Sim JE, Spitz DR, Wilson GL, LeDoux SP. Glial cell type-specific responses to menadione-induced oxidative stress. *Free Radic Biol Med*. 2000;28:1161–74.
45. Xu B, Lang L-M, Li S-Z, Guo J-R, Wang J-F, Wang D, Zhang L-P, Yang H-M, Lian S: **Cortisol Excess-Mediated Mitochondrial Damage Induced Hippocampal Neuronal Apoptosis in Mice Following Cold Exposure**. *Cells* 2019, 8.
46. Voets AM, Huigsloot M, Lindsey PJ, Leenders AM, Koopman WJH, Willems PHGM, Rodenburg RJ, Smeitink JAM, Smeets HJM. Transcriptional changes in OXPHOS complex I deficiency are related to anti-oxidant pathways and could explain the disturbed calcium homeostasis. *Biochim Biophys Acta*. 2012;1822:1161–8.

47. Vianna MR, Alonso M, Viola H, Quevedo J, de Paris F, Furman M, de Stein ML, Medina JH, Izquierdo I. Role of hippocampal signaling pathways in long-term memory formation of a nonassociative learning task in the rat. *Learning memory (Cold Spring Harbor NY)*. 2000;7:333–40.
48. Baumgartner HK, Gerasimenko JV, Thorne C, Ashurst LH, Barrow SL, Chvanov MA, Gillies S, Criddle DN, Tepikin AV, Petersen OH, et al. Caspase-8-mediated apoptosis induced by oxidative stress is independent of the intrinsic pathway and dependent on cathepsins. *American journal of physiology Gastrointestinal liver physiology*. 2007;293:G296–307.
49. Vannucci RC, Brucklacher RM, Vannucci SJ. Intracellular calcium accumulation during the evolution of hypoxic-ischemic brain damage in the immature rat. *Brain research Developmental brain research*. 2001;126:117–20.
50. Baumgartner HK, Gerasimenko JV, Thorne C, Ferdek P, Pozzan T, Tepikin AV, Petersen OH, Sutton R, Watson AJM, Gerasimenko OV. Calcium elevation in mitochondria is the main Ca²⁺ requirement for mitochondrial permeability transition pore (mPTP) opening. *J Biol Chem*. 2009;284:20796–803.
51. Mayer SI, Müller I, Mannebach S, Endo T, Thiel G. Signal transduction of pregnenolone sulfate in insulinoma cells: activation of Egr-1 expression involving TRPM3, voltage-gated calcium channels, ERK, and ternary complex factors. *J Biol Chem*. 2011;286:10084–96.
52. Phelps ED, Sweeney KR, Blader IJ. *Toxoplasma gondii* rhoptry discharge correlates with activation of the early growth response 2 host cell transcription factor. *Infect Immun*. 2008;76:4703–12.
53. Hsiao H-W, Liu W-H, Wang C-J, Lo Y-H, Wu Y-H, Jiang S-T, Lai M-Z. Deltex1 is a target of the transcription factor NFAT that promotes T cell anergy. *Immunity*. 2009;31:72–83.
54. Wang J, Pantopoulos K. Regulation of cellular iron metabolism. *Biochem J*. 2011;434:365–81.
55. Singh N, Haldar S, Tripathi AK, Horback K, Wong J, Sharma D, Beserra A, Suda S, Anbalagan C, Dev S, et al. Brain iron homeostasis: from molecular mechanisms to clinical significance and therapeutic opportunities. *Antioxid Redox Signal*. 2014;20:1324–63.
56. Labunskyy VM, Gladyshev VN. Role of reactive oxygen species-mediated signaling in aging. *Antioxid Redox Signal*. 2013;19:1362–72.
57. Hui Y, Wang D, Li W, Zhang L, Jin J, Ma N, Zhou L, Nakajima O, Zhao W, Gao X. Long-term overexpression of heme oxygenase 1 promotes tau aggregation in mouse brain by inducing tau phosphorylation. *Journal of Alzheimer's disease: JAD*. 2011;26:299–313.
58. Wu J, Yang J-J, Cao Y, Li H, Zhao H, Yang S, Li K. Iron overload contributes to general anaesthesia-induced neurotoxicity and cognitive deficits. *J Neuroinflamm*. 2020;17:110.
59. Eaton JW, Qian M. Molecular bases of cellular iron toxicity. *Free Radic Biol Med*. 2002;32:833–40.
60. Richardson DR, Lane DJR, Becker EM, Huang MLH, Whitnall M, Suryo Rahmanto Y, Sheftel AD, Ponka P. Mitochondrial iron trafficking and the integration of iron metabolism between the mitochondrion and cytosol. *Proc Natl Acad Sci USA*. 2010;107:10775–82.
61. Rosa P, Zerbinati C, Crestini A, Canudas A-M, Ragona G, Confaloni A, Iuliano L, Calogero A. Heme Oxygenase-1 and Brain Oxysterols Metabolism Are Linked to Egr-1 Expression in Aged Mice Cortex, but Not in Hippocampus. *Front Aging Neurosci*. 2018;10:363.

62. Cellier MFM. **Developmental Control of NRAMP1 (SLC11A1) Expression in Professional Phagocytes.**
Biology 2017, 6.

Tables

Due to technical limitations, table 1 to 4 is only available as a download in the Supplemental Files section.

Figures

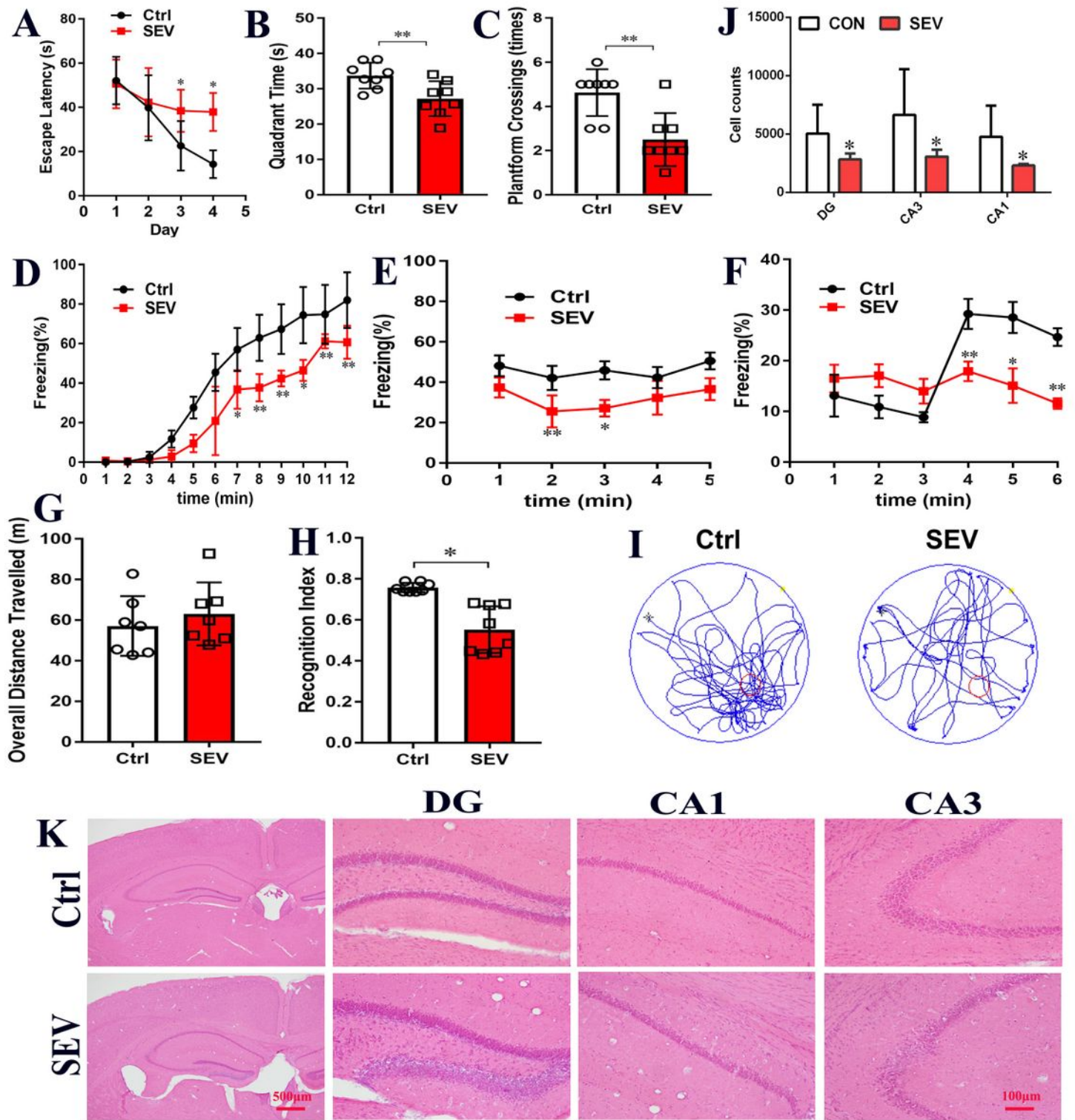


Figure 1

The behavioral performance and HE staining (A-C, I) Morris water maze test including the time course of escape latency, the time spent in the target quadrant and the times crossing the hidden platform, and moving track; (D-F) Freezing behavior detected by fear condition test; (G, H) Novel object recognition comprising of the overall distance of traveling and the recognition index; (J, K) HE staining and

quantitative analysis for cell counts. Scar bar = 500/100 μm , applied in Fig K. * $P < 0.05$, ** $P < 0.01$, Ctrl VS SEV.

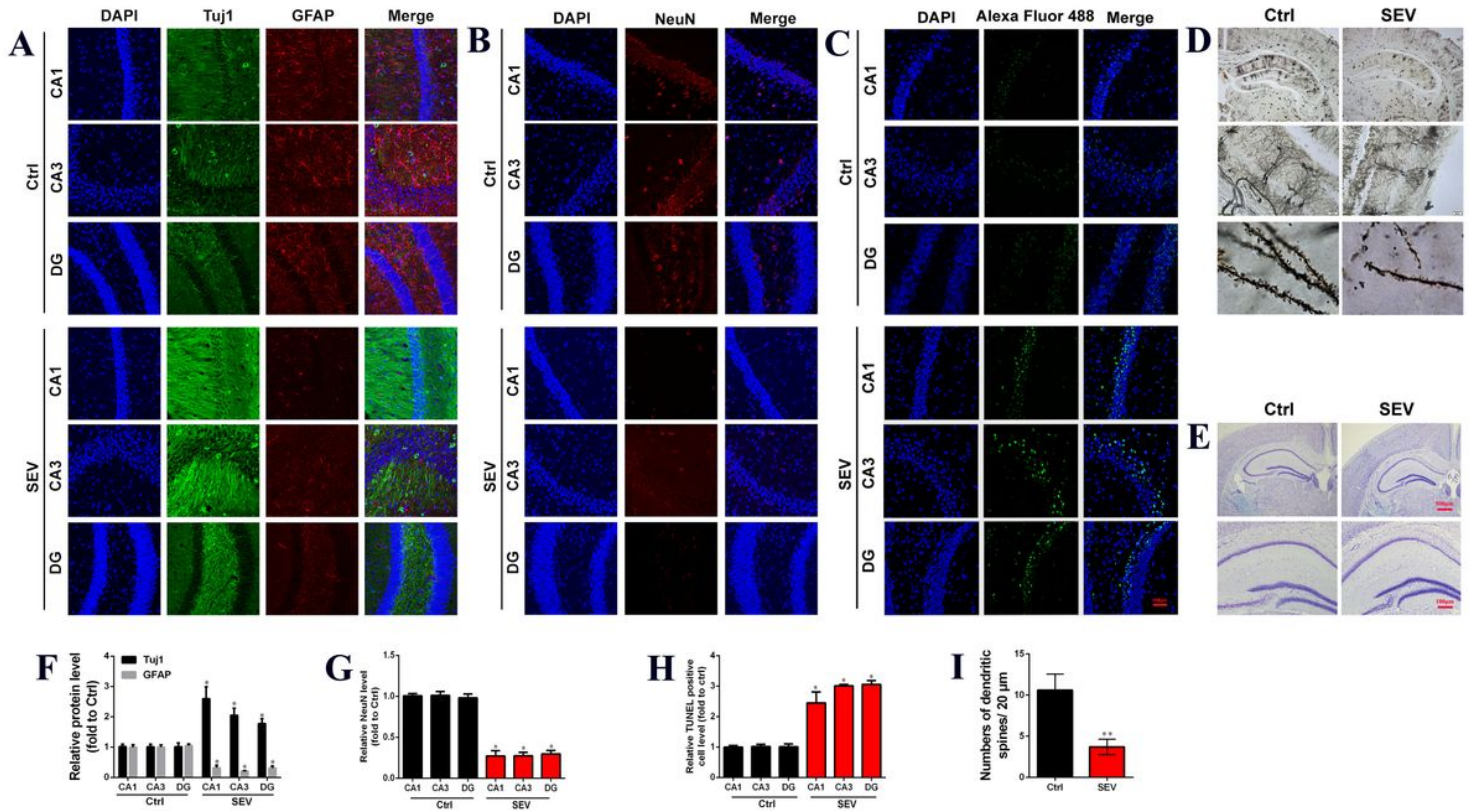


Figure 2

Sevoflurane administration induced the neuronal death and reduced the synapse formation in hippocampus (A-B) Expression of neuron-specific TuJ1 and NeuN in hippocampus indicated by immunofluorescent staining; (C) Cell apoptosis detection by Alexa Fluor 488 reagent; (D) Representative images of Golgi-Cox staining sections in hippocampus; (E) Representative photomicrographs of Nissl staining; (F-I) Quantitative results for TuJ1, GFAP, NeuN, TUNEL staining, and Golgi-Cox staining, respectively. Scar bar = 100 μm , applied in Fig A-C; Scar bar = 500/100 μm , applied in Fig E. * $P < 0.05$, ** $P < 0.01$, Ctrl VS SEV.

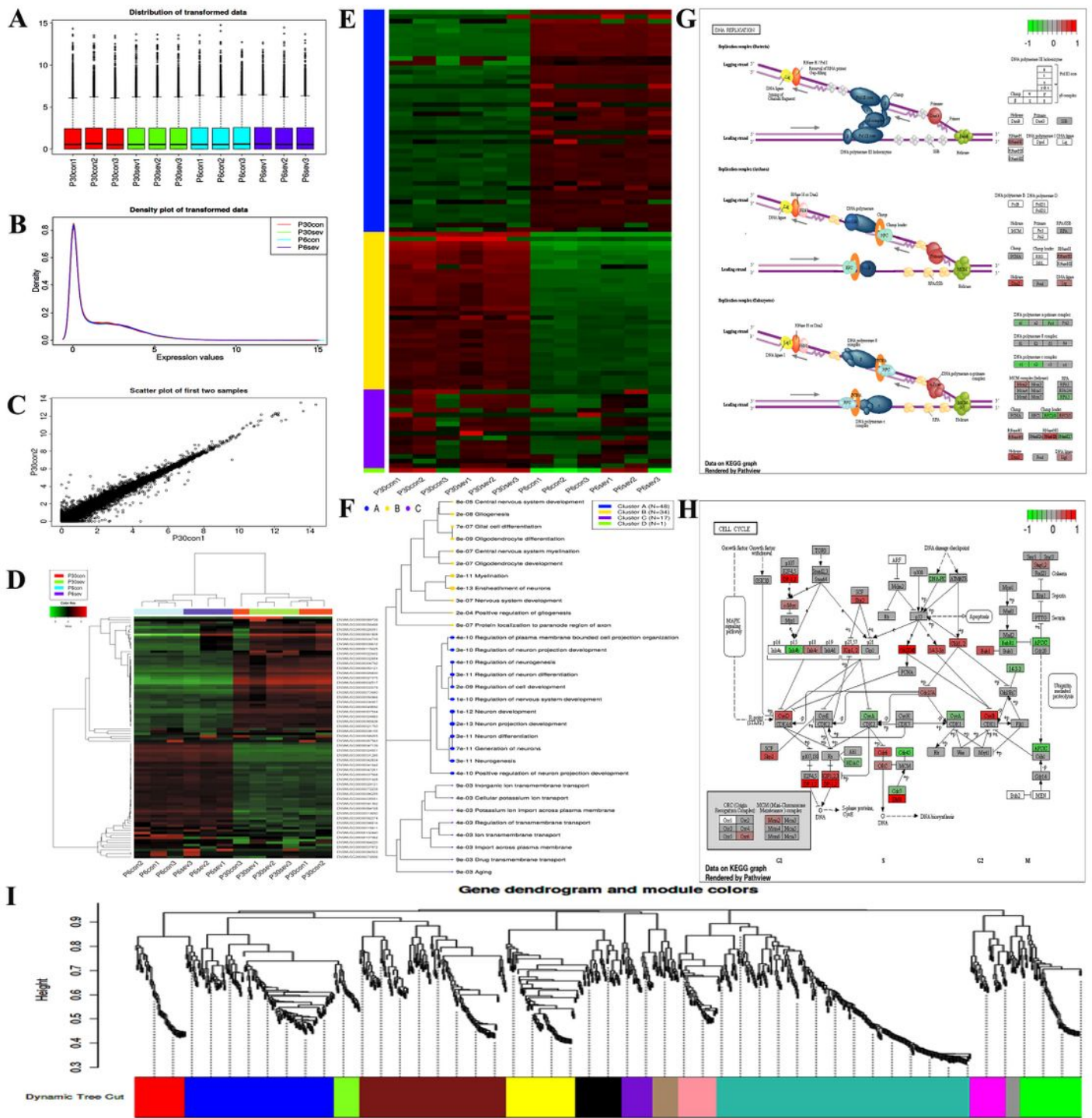


Figure 3

Bioinformatics analysis for RNA-Seq data (A) Boxplot of transformed data; (B) Distribution of transformed data utilizing a density plot; (C) Scatter plot of the first two samples; (D) Hierarchical clustering of top 100 genes, and the color scale represents the relative genes expression in certain slide: green indicates low relative expression levels; red indicates high relative expression levels; black indicates zero (No change); (E) K-means clustering; (F) Enrichment analysis for Go terms, Sizes of dot correspond

to adjusted P values; (G, H) Parametric analysis of gene set enrichment (PGSEA) for the potential interaction networks and signaling pathways involved in DNA replication and cell cycle; (I) Weighted gene correlation network analysis (WGCNA) for investigating the underlying correlations amongst genes and groups using network topology.

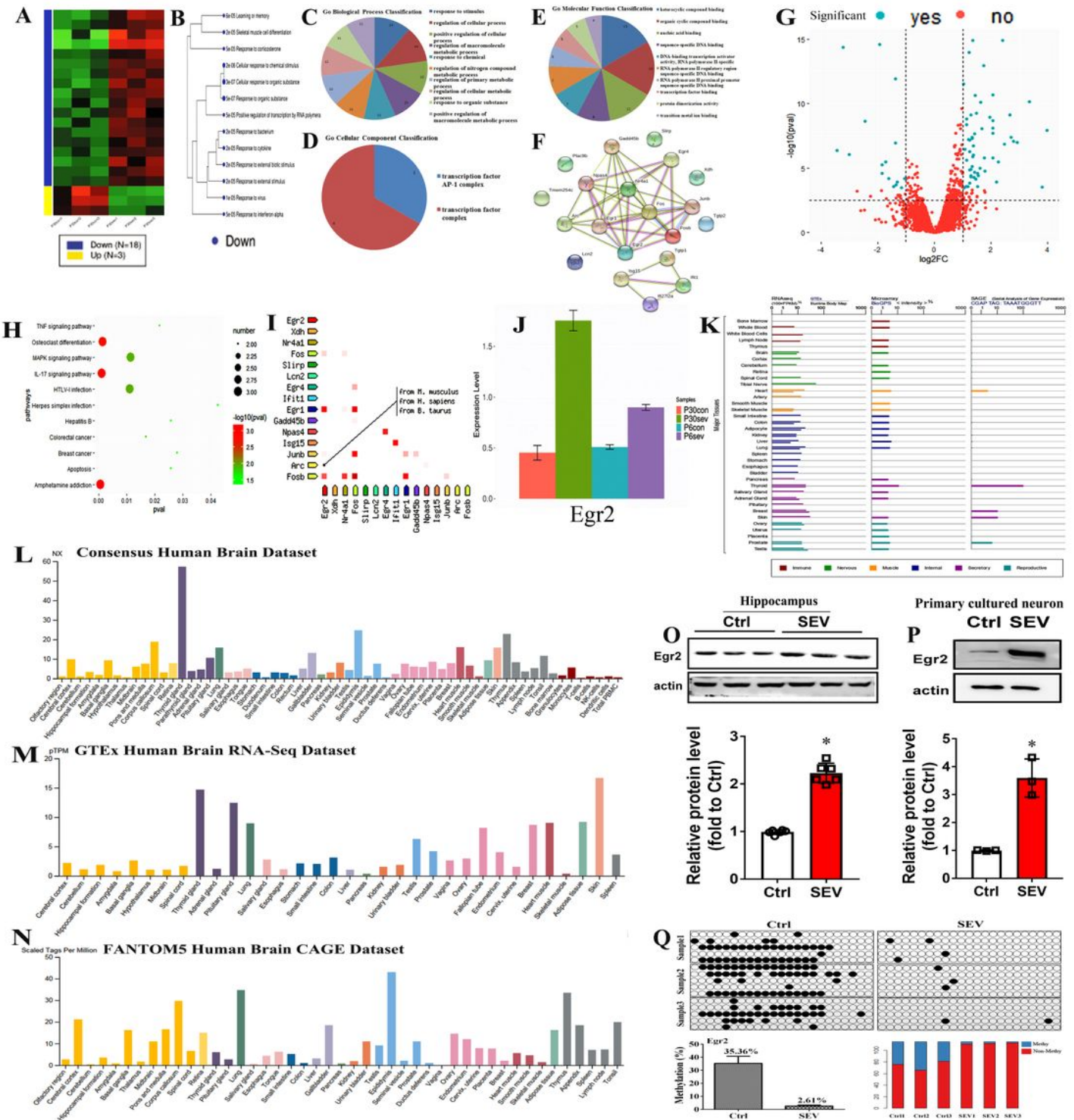


Figure 4

Sevoflurane administration results in the Egr2 expression upregulation (A-B) Cluster analysis of DEGs for heat map and dendrogram; (C-F) GO function analysis including biological process (BP), cellular component (CC), and molecular function (MF), and the PPI network construction; (G) The volcano plot for displaying the distribution of DEGs; (H) Bubble plot showed the related signal pathways based on GO analysis; x-axis represents the P value and y-axis describe the enrichment components. The area of the circle is proportional to the number of genes assigned to the term and the color accords with the P value; (I) Gene coexpression analysis was identified by String tools; (I) The expression level of Egr2 at P6 and P60 obtained from RNA-Seq; (K-N) The Egr2 expression in different tissues resulted from Genecards database and The Human Protein Atlas website; (O, P) WB assay for detecting the relative protein level of Egr2 in animal hippocampus and primary cultured neuron, respectively; (Q) Bisulfite sequencing PCR (BSP) technique for measuring the percentage of methylated CpGs in Egr2. *P < 0.05, Ctrl VS SEV.

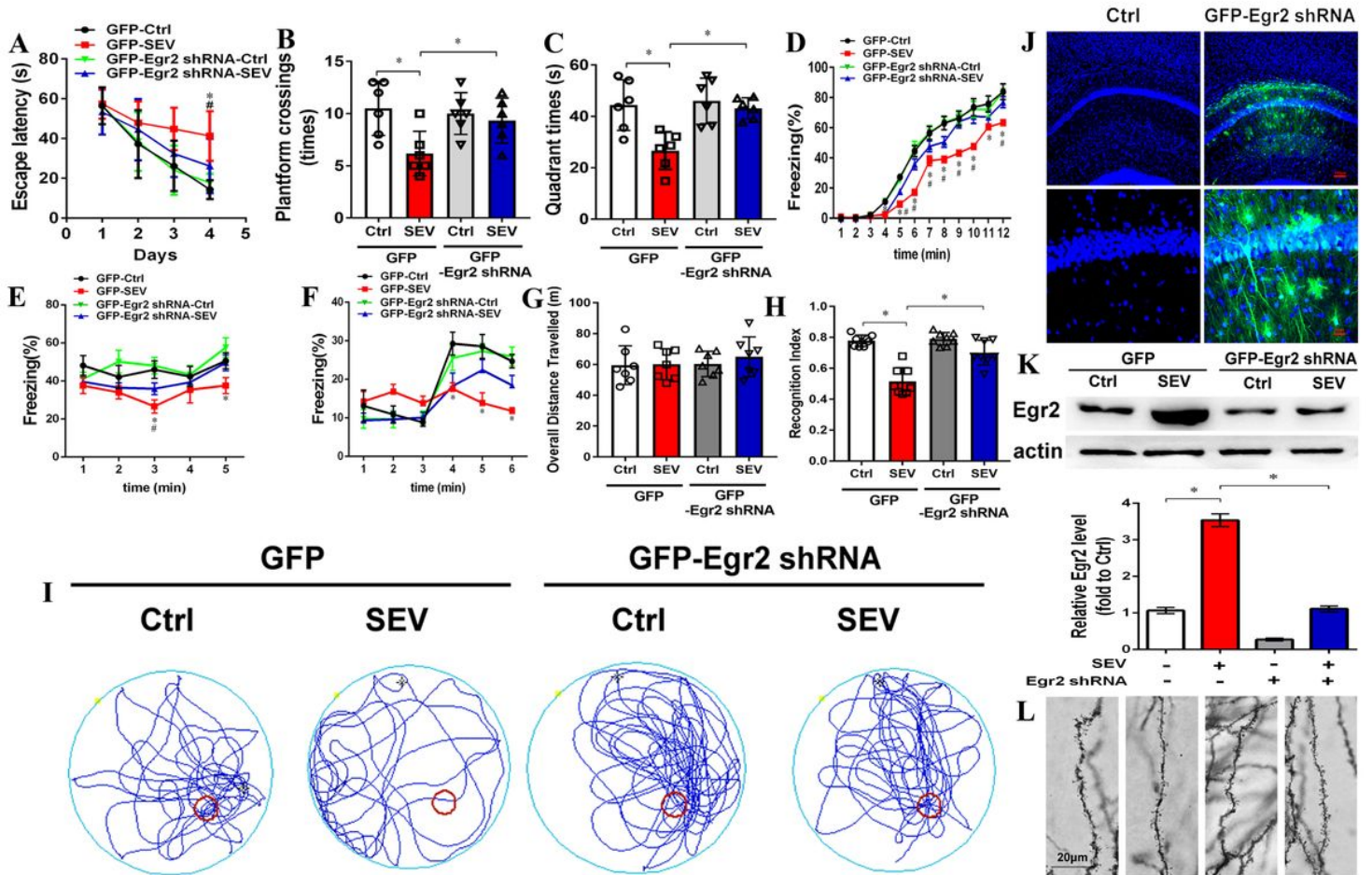


Figure 5

Egr2 downregulation alleviated the cognitive deficits induced by sevoflurane administration (A-C, I) Morris water maze test consisting of the time course of escape latency, the time spent in the target quadrant, the times crossing the hidden platform and motion trail; (D-F) Freezing behavior detected by fear condition test; (G, H) Novel object recognition comprising of the overall distance of traveling and the recognition index; (J) The transfection of recombinant adeno-associated virus (AAV) in the hippocampus by intracerebroventricular injection; (K) WB assay for detecting the Egr2 protein level; (L) Representative

images of Golgi-Cox staining sections in hippocampus. Scar bar = 100/30 μm , applied in Fig J; Scar bar = 20 μm in Fig L. * $P < 0.05$, GFP-Ctrl VS GFP-SEV; # $P < 0.05$, GFP-Egr2 shRNA-SEV VS GFP-SEV.

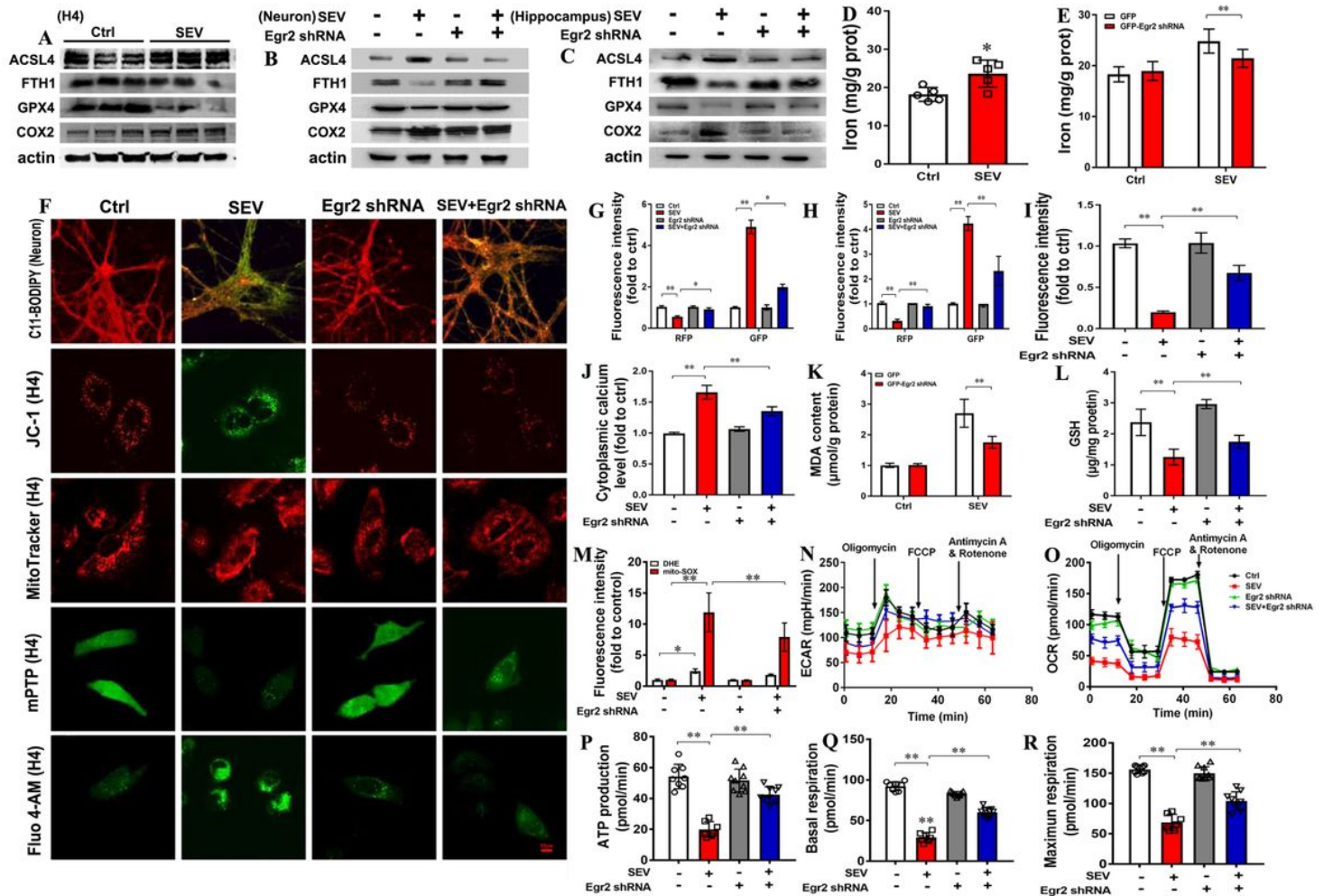


Figure 6

Sevoflurane administration elicits iron overload and mitochondrial dysfunction associated with Egr2 upregulation (A-C) WB assay for detecting iron metabolism-related proteins; (D, E) Iron content detection; (F-J) Immunofluorescent staining by using C11-BODIPY staining, JC-1 probe, MitoTracker staining, Mitochondrial permeability transition pore assay, and Fluo calcium indicators to investigate the level of lipid peroxidation, mitochondrial membrane potential, morphology and membrane permeability, and cytoplasm calcium levels, respectively; (K, L) Detection for the level of MDA and GSH; (M) The DHE and mito-SOX staining for measuring the level of intracellular and mitochondrial ROS; (N-R) Aerobic respiration and anaerobic glycolysis detection including ECAR and OCR assay. Scar bar = 10 μm , applied in Fig F.* $P < 0.05$, ** $P < 0.01$.

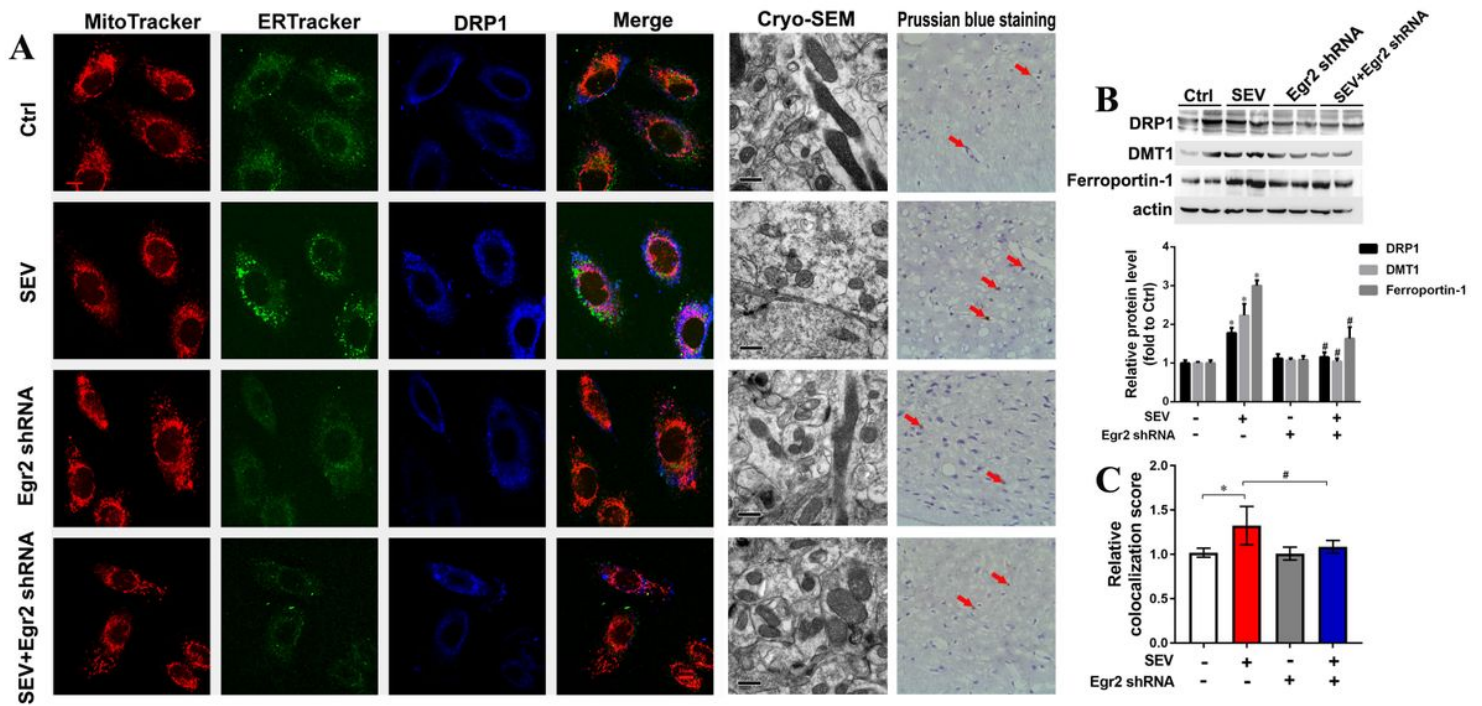


Figure 7

Egr2 downregulation alleviates iron overload-induced ER-mediated mitochondrial fission in hippocampal primary neurons (A) Immunofluorescent staining, Cryo-electron microscopy observation and Prussian blue staining for detecting the correlation between Egr2 expression and iron overload-induced mitochondrial fission, mitochondrial morphology and iron deposition, respectively; (B) WB assay for detecting iron metabolism and mitochondrial fission-related proteins; (C) Manders' overlap coefficient (MOC) was calculated to determine the degree of colocalization. Scar bar = 10 or 5 μ m, applied in Fig A for immunofluorescent staining or Cryo-electron microscopy observation, respectively. Red arrow indicates the positive cells of Prussian blue staining. *P < 0.05, GFP-Ctrl VS GFP-SEV; #P < 0.05, GFP-Egr2 shRNA-SEV VS GFP-SEV.

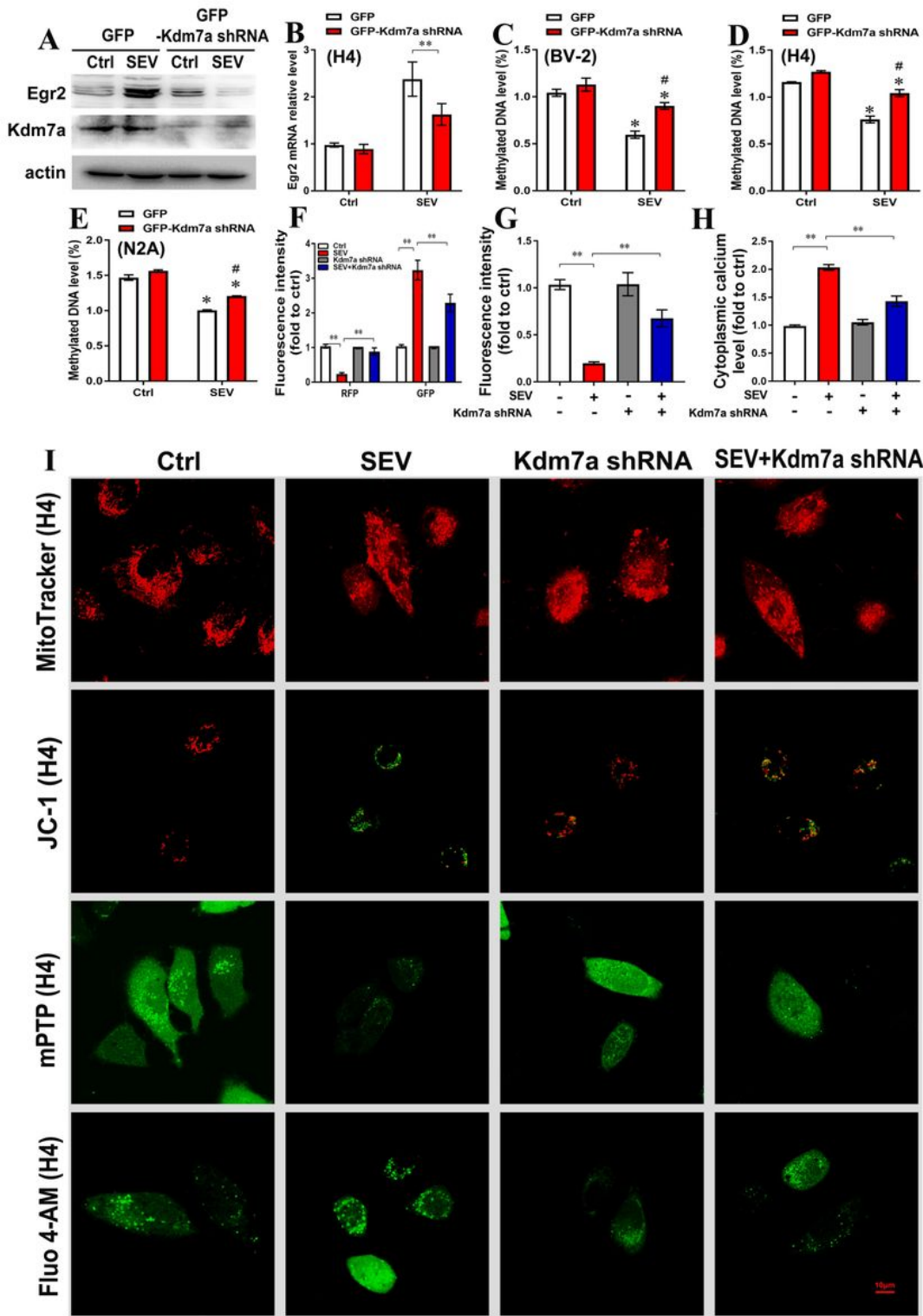


Figure 8

Kdm7a gene expression silencing mediated Egr2 level correlated to the reverse mitochondria dysfunction (A) WB assay for detecting the protein level of Kdm7a and Egr2; (B) The mRNA expression of Egr2 by PCR; (C-E) The methylated DNA level was detected following Kdm7a gene expression silencing; (F-I) The mitochondrial morphology, membrane potential, membrane permeability, and cytoplasm calcium levels were assessed by MitoTracker staining, JC-1 probe, Mitochondrial permeability transition pore assay, and

Fluo calcium indicators, respectively. Scar bar = 10 μ m, applied in Fig I. *P < 0.05, **P < 0.01; (C-E) *P < 0.05, GFP-Ctrl VS GFP-SEV; #P < 0.01, GFP-Egr2 shRNA-SEV VS GFP-SEV.

Supplementary Files

This is a list of supplementary files associated with this preprint. Click to download.

- [Table1.csv](#)
- [Table1.csv](#)
- [Table1.csv](#)
- [Table1.csv](#)
- [Table2.csv](#)
- [Table2.csv](#)
- [Table2.csv](#)
- [Table2.csv](#)
- [Table3.csv](#)
- [Table3.csv](#)
- [Table3.csv](#)
- [Table3.csv](#)
- [Table4.csv](#)
- [Table4.csv](#)
- [Table4.csv](#)
- [Table4.csv](#)
- [TableS1.csv](#)
- [TableS1.csv](#)
- [TableS1.csv](#)
- [TableS1.csv](#)
- [TableS2.csv](#)
- [TableS2.csv](#)
- [TableS2.csv](#)
- [TableS2.csv](#)
- [TableS3.docx](#)
- [TableS3.docx](#)
- [TableS3.docx](#)
- [TableS3.docx](#)